

UNIMORE

UNIVERSITÀ DEGLI STUDI DI
MODENA E REGGIO EMILIA

Department of Engineering Sciences and Methods

Master's Degree Course in Digital Automation Engineering

Simulation of convective heat transfer around oil-cooled electrical windings

Supervisors:
Prof. Diego Angeli

Co-supervisor:
Ludovico campanelli

Candidate:
Muhammad sohaib

Academic Year 2025/2026

Table of Contents

Table of Contents 2
Acknowledgements 5
Abstract 6
Nomenclature 7
Power Transformers 8
1.1 Constructional overview 8
1.1.1 Conductors 9
1.1.2 Core 9
1.1.3 Insulation 10
1.2 Oil-immersed transformers 10
1.2.1 Oil as an insulant 11
1.2.2 Oil as a coolant 11
1.2.3 Types of oil used 11
1.3 Thermal effects and cooling 12
1.3.1 Heat exchange in transformers 12
1.3.2 Cooling arrangements 12
1.3.3 Ageing of insulation and operating life 13
1.4 Thermal analysis 14
1.4.1 Analytical methods 14
1.4.2 Direct measurement 14
1.4.3 Numerical methods 14
1.5 Dimensionless groups in natural-convection cooling 15
Case Study 16
2.1 Description of the geometry 16
2.2 Governing equations 16
2.3 Boundary and operating conditions 17
2.4 Mesh independence considerations 17
Numerical Methodology 19
3.1 Mesh generation workflow 19
3.2 Solver and discretisation schemes 20
3.3 Validation reference 20
3.4 Discretisation schemes 21
3.5 Verification metrics 21
3.6 Practical implementation lessons 22
3.6.1 Region-splitting and coupled-interface consistency 22

3.6.2 Mesh-quality verification 22
3.6.3 Solver-specific requirements 22
Porting and Validation of the Single-Pass Model (Task 1) 24
4.1 Objectives 24
4.2 Coarse mesh 24
4.2.1 Convergence history 26
4.3 Sampling methodology 26
4.4 Coarse-mesh quantitative comparison with the foam-extend reference 26
4.4.1 Fluid region 26
4.4.2 Solid regions 28
4.4.3 Summary 29
4.5 Field-contour visualisation, coarse mesh 29
4.6 Refined mesh 31
4.6.1 Convergence history 32
4.7 Discussion 33
Two-Pass Extension: Variable-Properties and Boussinesq Comparison (Task 2) 34
5.1 Objectives and physical models 34
5.2 Two-pass mesh development 34
5.3 Numerical setup and convergence criteria 35
5.3.1 Variable-properties (VP) model 35
5.3.2 Boussinesq model 36
5.4 Heat-source correction 36
5.5 Mesh 36
5.6 Convergence Behaviour 37
5.7 Task 2a: VP vs. Boussinesq Comparison 37
5.7.1 Quantitative agreement 37
5.7.2 Field contours 41
5.8 Task 2b: Analytical Boussinesq Validity Assessment 43
5.8.1 Criterion 43
5.8.2 Interpretation 44
5.9 Discussion 45
5.10 Refined Mesh 45
5.10.1 Field contours 45
5.10.2 Why no Task 2b assessment yet 47
5.11 Summary 48
Conclusions 49
6.1 Summary of findings 49

6.2 Future work 50
Bibliography 51

Acknowledgements

I would like to express my sincere gratitude to my supervisor, Prof. Diego Angeli, for giving me the opportunity to carry out this thesis within the research group of the Department of Engineering Sciences and Methods (DISMI) of the University of Modena and Reggio Emilia. His guidance, his scientific rigour and his readiness to discuss the physical meaning of the results, and not only the numerical ones, shaped the way I approached this work.

My special thanks go to co-supervisor Ludovico Campanelli, whose day-to-day technical support was decisive at every stage of the project. Their availability and patience allowed me to learn a new simulation environment while working on a demanding conjugate heat transfer problem. They provided the custom Boussinesq library used in the second part of this thesis, reviewed my case set-ups and convergence behaviour, and identified two errors that would otherwise have gone unnoticed: the loosely defined convergence criteria in the first set of simulations, and the incorrect scaling of the heat source in the two-pass model. Each of these observations led to a real improvement in the quality of the results, and I learned from them that a well-converged simulation is not necessarily a correct one.

This thesis builds on the earlier work of the research group on the same disc-type winding geometry. In particular, I am indebted to the authors of the published comparative studies of the Boussinesq approximation, Torriano, Salerno and co-workers, and to the authors of the previous master's theses developed within the group. Their reference case, correlations and results provided the foundation on which the porting, validation and extension described here were built.

I also wish to thank the University of Modena and Reggio Emilia and the teaching staff of the Master's Degree in Digital Automation Engineering for the education I received during these years.

Abstract

Power transformers reject the heat generated by core and winding losses primarily through the natural convection of the surrounding insulating oil, and accurate prediction of the resulting winding hot-spot temperature is central to transformer thermal design. This thesis addresses two related computational fluid dynamics tasks on a disc-type low-voltage winding of an oil-immersed power transformer, building on the reference case studied by Torriano and by Salerno et al.

The first task ports an existing single-pass, two-dimensional conjugate heat transfer model of the winding from foam-extend 4.0 to OpenFOAM v2306, on both a coarse and a refined computational mesh, and validates the ported solution quantitatively against the original foam-extend results. A specific, previously undocumented mesh-generation methodology is developed to correctly produce OpenFOAM-compatible axisymmetric wedge meshes from a Pointwise export. The ported solution is found to reproduce the fluid-region temperature and velocity fields closely, while a larger, well-diagnosed solid-region temperature gap is attributed to differing degrees of thermal equilibration between the two solver runs rather than to any modelling error.

The second task extends the validated methodology to a two-pass winding geometry, building a constant-property Boussinesq buoyancy model and a more complete variable-thermophysical-properties model on the same corrected two-pass mesh, boundary conditions and heat source, in order to assess the applicability of the Boussinesq approximation to this problem. On the converged coarse-mesh case, the two models predict closely agreeing temperature and velocity fields (mean absolute temperature differences of 0.6–1.9 K across the sampled lines), but a full assessment against the analytical validity criterion of Gray and Giorgini (1976), applied to all four relevant thermophysical properties rather than density alone, finds that the Boussinesq approximation is not formally valid over this two-pass domain, driven primarily by the strong temperature-dependence of the oil's viscosity, and secondarily by density variation concentrated near the hottest disc surfaces. This distinction between close numerical agreement and formal theoretical invalidity, a more complete picture than a density-only check would suggest, is a central conclusion of this work, and contrasts with the full four-pass winding studied in the literature, where the much larger associated temperature range was found to push even the density criterion itself into formal invalidity. A refined two-pass mesh (≈4.1× the coarse cell count) was built and verified to run correctly with the same corrections applied, but could not be advanced beyond an early-transient state before the submission deadline, so the refined-mesh comparison remains preliminary.

Keywords: power transformer, natural convection, conjugate heat transfer, OpenFOAM, Boussinesq approximation,disc-type winding.

Nomenclature

Symbol	Meaning (SI unit)
T	Temperature (K)
U, u	Velocity vector (m/s)
p	Static pressure (Pa)
p_rgh	Pseudo-hydrostatic (buoyancy-reduced) pressure, p_rgh = p − ρ g·h (Pa)
ρ	Density (kg/m³)
μ	Dynamic viscosity (Pa·s)
ν	Kinematic viscosity, ν = μ/ρ (m²/s)
k	Thermal conductivity (W/(m·K))
Cp	Specific heat at constant pressure (J/(kg·K))
α	Thermal diffusivity, α = k/(ρ Cp) (m²/s)
β	Thermal expansion coefficient (K^{-1})
g	Gravitational acceleration (m/s²)
Tref	Reference temperature for the Boussinesq approximation (K)
Gr	Grashof number
Pr	Prandtl number
Ra	Rayleigh number, Ra = Gr·Pr
ΔT	Characteristic temperature difference (K or °C)
$\dot{Q}$	Volumetric or total heat generation rate (W or W/m³)
CHT	Conjugate heat transfer
LV	Low voltage
ONAN / ONAF / OFAF / ODAF	Transformer cooling-class designations (Section 1.3.2)
OF	OpenFOAM v2306 (used as a column label in Tables 4.2 and 4.4)
FE	foam-extend 4.0, the reference solver (used as a column label in Tables 4.2 and 4.4)
VP	Variable (thermophysical) properties model (Chapter 5)

Chapter 1

Power Transformers

1.1 Constructional overview

A power transformer is a static electrical machine that transfers electrical energy between two or more circuits through electromagnetic induction, changing voltage and current levels while ideally leaving the transmitted power unchanged. Power transformers are a cornerstone of electrical transmission and distribution networks: step-up units raise the voltage of generated power for efficient long-distance transmission, while step-down units lower it again for distribution to industrial and residential loads. Although modern power transformers are highly efficient machines, with efficiencies typically in excess of 99%, the fraction of the transmitted power that is not converted is dissipated as heat within the active parts of the machine. Because the temperatures reached in these regions govern the reliability and the operating life of the transformer, the design of an adequate cooling system is one of the central problems in transformer engineering, and is the subject of this thesis.

The active part of a transformer consists of a magnetic core, usually built from stacked or wound laminations of grain-oriented electrical steel, around which one or more sets of windings are arranged. In a typical two-winding power transformer, a low-voltage (LV) winding and a high-voltage (HV) winding are wound concentrically around the same core limb, electrically insulated from one another and from the core, and mechanically supported by pressboard and other cellulose-based insulating structures. Section 1.1.1 discusses the winding conductors themselves, Section 1.1.2 the magnetic core, and Section 1.1.3 the insulation system in more detail.

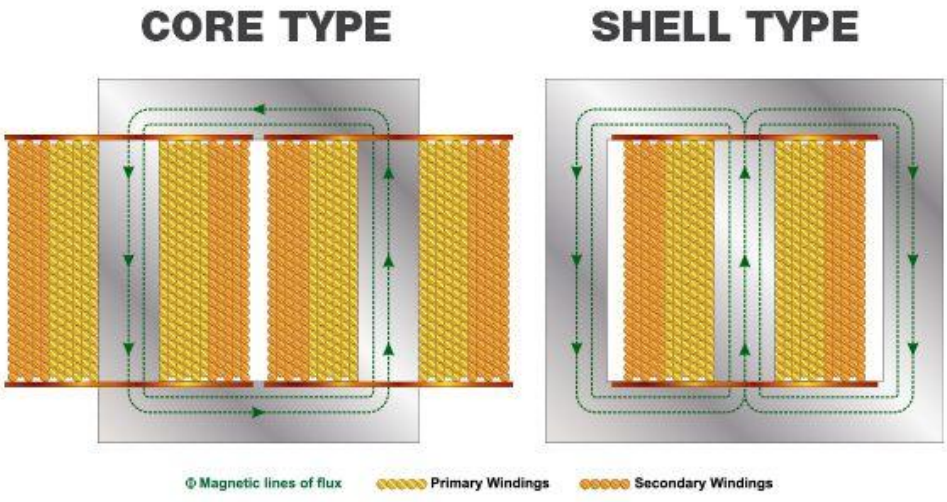


Figure 1.1: Core-type and shell-type transformer configurations.

From a thermal-modelling perspective, the distinction between core-type and shell-type construction is relevant because the arrangement of the active parts determines the available cooling paths and the relative position of the winding surfaces with respect to the surrounding oil. The reference thesis distinguishes these two principal constructional configurations and further identifies layer, helical and disc arrangements as common winding geometries. The present work focuses specifically on a disc-type winding, for which the axial and radial cooling ducts form an important part of the thermal-fluid problem [7].

1.1.1 Conductors

The winding conductors are almost always made of copper or aluminium, chosen for their high electrical conductivity. Copper remains the more common choice in medium- and large-power transformers because of its superior conductivity per unit cross-section and its favourable mechanical properties, despite its higher cost and density relative to aluminium. Conductors are shaped as round wire, rectangular strip, or, for higher-current applications, as continuously transposed cable (CTC) bundles of multiple parallel strands designed to reduce eddy-current losses caused by the leakage flux linking the winding.

Windings are built up from a number of concentric layers or discs of conductor, separated by radial and axial cooling ducts that allow the coolant (oil, in the case considered in this thesis) to flow past the conductor surface and remove the heat generated by Joule losses. The disc-type winding, in which the conductor is wound into a stack of flat pancake-shaped discs separated by axial ducts and interleaved with radial spacers, is one of the most widely used configurations in medium- and high-voltage windings and is the configuration adopted for the case study of this thesis, described in detail in Chapter 2.

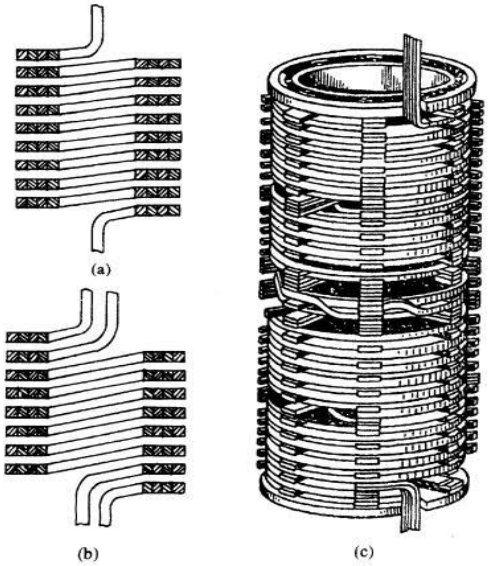


Figure 1.2: Disc-type transformer winding, illustrating the stacked disc arrangement and radial cooling spacers.

In a disc winding, one or more insulated conductor strips are wound into discs arranged successively along the axial direction. The discs are connected through alternating crossover locations, while insulating spacers maintain the cooling passages between adjacent discs. This arrangement creates a repeated network of narrow oil channels in which buoyancy-driven circulation develops as the oil is heated by the winding losses. Consequently, the winding geometry simultaneously controls both the conduction path through the solid insulation and the hydraulic resistance experienced by the cooling oil [7].

1.1.2 Core

The magnetic core provides the low-reluctance path required to link the magnetic flux between the primary and secondary windings. It is built from thin, mutually insulated laminations of cold-rolled, grain-oriented silicon steel (silicon content around 3%, chosen for its low magnetostriction and high permeability), typically 0.23–0.35 mm thick, stacked so as to minimise eddy-current losses induced by the time-varying flux; because resistivity across the lamination stack is far higher than within a single sheet, the core's effective thermal conductivity is itself anisotropic, favouring conduction along the lamination plane over conduction through the stack. Core losses comprise hysteresis losses, which scale approximately with frequency and with peak flux density raised to the Steinmetz exponent ($P_h \propto f \cdot B_{max}^n$, typically

$n \approx 1.6–2.0$), and eddy-current losses, which scale with the square of frequency, lamination thickness and peak flux density ($P_e \propto f^2 \cdot t^2 \cdot B_{max}^2$); modern power-transformer cores normally operate at a peak flux density of about 1.6–1.75 T, close to the steel's saturation limit, to minimise core mass and cost for a given rating [10]. Together with the winding's Joule (copper) losses, core losses constitute the two principal heat sources inside an operating transformer. In the present work, however, the core itself lies outside the modelled fluid–solid domain (Section 2.1), and its contribution to the oil temperature is captured only implicitly, through the prescribed temperature of the oil entering the winding at the inlet, rather than through an explicit core heat source.

1.1.3 Insulation

Electrical insulation must be provided between turns, between discs, between windings, and between each winding and the core and tank. In oil-immersed transformers the insulation system is a composite one, combining a solid, cellulose-based component, typically kraft paper or pressboard, wrapped around the conductor or used as spacers and barriers, with a liquid component, the insulating oil that fills the remaining free volume inside the tank. Both must satisfy demanding dielectric requirements while also playing an active role in the thermal management of the machine: the oil acts simultaneously as a dielectric medium and as the working fluid of the cooling system, while the solid cellulose insulation, having a much lower thermal conductivity than either the metal conductor or the oil, is frequently the single largest thermal resistance in the conduction path between the heat-generating conductor and the oil-side convective boundary layer, a point of direct relevance to the conjugate heat transfer analysis carried out in this thesis, since the paper wrap around each copper conductor is explicitly resolved in the computational model.

The combined thermal and electrical duty of the cellulose insulation also governs the ageing of the transformer as a whole. Excessive sustained temperatures accelerate the chemical degradation of the paper, progressively reducing its mechanical strength and, ultimately, its ability to withstand the electrodynamic forces generated during short-circuit events; this ageing process is discussed further in Section 1.3.3.

1.2 Oil-immersed transformers

Oil-immersed transformers, in which the active part is fully submerged in a bath of insulating liquid contained within a sealed steel tank, are the dominant construction for medium- and large-power transformers, owing to the combined dielectric and cooling function that the oil provides (Section 1.2.1 and Section 1.2.2 respectively). The tank is typically fitted with an expansion (conservator) vessel, or built as a fully sealed, hermetically gas-blanketed unit for smaller ratings, so as to accommodate the oil's thermal expansion while limiting its exposure to atmospheric oxygen and moisture, both of which accelerate oil and paper ageing (Section 1.3.3); a network of external radiators, sized according to the transformer's cooling class (Section 1.3.2), provides the additional heat-rejection surface that the tank walls alone cannot supply once unit ratings exceed a few MVA. Dry-type transformers, which rely on air or a solid cast-resin insulation system instead, dispense with this liquid entirely and are generally reserved for lower-power, indoor applications (typically distribution-class units up to a few MVA, installed in buildings, ships or mines) where fire safety or environmental constraints make the use of a liquid dielectric undesirable, at the cost of a lower achievable power density and a more limited maximum rating than the oil-immersed design considered throughout the remainder of this thesis.

1.2.1 Oil as an insulant

The primary electrical function of the insulating oil is to provide a dielectric medium with a breakdown strength substantially higher than that of air, allowing the physical clearances between live parts, and hence the overall size of the transformer, to be reduced relative to an air-insulated design. In combination with

the solid cellulose insulation described in Section 1.1.3, the oil forms a composite dielectric system in which the oil primarily withstands the electric field across the larger, oil-filled gaps between windings and between winding and tank, while the paper and pressboard provide localised reinforcement at points of highest stress, such as sharp conductor edges and winding-to-core clearances. Because oil's dielectric strength is far more sensitive to dissolved moisture and gas than that of paper, oil dryness and degassing are treated as safety-critical during manufacture, commissioning and maintenance; moisture ingress is one of the principal reasons for the sealed or conservator-protected tank construction discussed in Section 1.2.

A suitable insulating oil must combine a low viscosity, to promote convective circulation and heat removal; a low pour point, to remain fluid at the lowest ambient temperatures the transformer may experience; a high flash point and fire point, for safety; excellent chemical stability, to resist oxidation and the formation of sludge over decades of service; a high dielectric strength; and a low density. Viscosity and dielectric performance are both temperature-dependent: viscosity falls sharply as the oil warms, which is part of why the natural-convection cooling flow strengthens as the winding heats up, while dielectric strength itself degrades with age as oxidation by-products and moisture accumulate, linking the oil's insulating performance directly to the ageing process discussed in Section 1.3.3.

International standards (IEC) classify insulating oils into three classes on the basis of flash point, pour point and kinematic viscosity at 40 °C, with Class I oils suited to temperate climates and Class II and III oils formulated for progressively colder operating environments; the mineral oil considered in this thesis, whose thermophysical properties are summarised in Table 2.1 (and, for the variable-properties model, in Section 5.1), corresponds to a standard Class I oil. Section 1.2.3 discusses the different chemical families of insulating liquid, mineral, natural ester and synthetic ester oils, in more detail.

1.2.2 Oil as a coolant

In addition to its dielectric role, the oil is the working fluid of the transformer's cooling system, and it is this function that is the central concern of the present thesis. Heat generated in the core and windings is transferred by conduction through the solid insulation to the oil-wetted surfaces, and thence carried away by the oil, either by buoyancy-driven natural convection alone (as in the oil natural, air natural, ONAN, cooling class discussed in Section 1.3.2) or with the assistance of pumps and external heat exchangers (forced or directed-flow cooling classes). The relatively low thermal conductivity of mineral oil, compared with water or other common coolants, is compensated by the very large wetted surface area presented by the winding conductors and by the favourable geometry of the cooling ducts, which are specifically designed and sized to promote an efficient natural-convection flow at the modest driving temperature differences typically available inside a transformer.

1.2.3 Types of oil used

Mineral oil, refined from naphthenic or paraffinic crude petroleum stocks, remains the most widely used insulating and cooling liquid in power transformers world-wide, owing to its well-established performance, moderate cost, and compatibility with decades of established manufacturing and maintenance practice. Synthetic alternatives, most notably silicone fluids and, more recently, natural and synthetic ester fluids, offer improved fire safety (substantially higher fire and flash points) and, in the case of ester fluids, biodegradability and a reduced environmental impact in the event of a spill, at the cost of higher viscosity and, generally, a higher purchase price. The physical properties adopted for the oil in the present numerical study (Chapter 2) correspond to a mineral-oil formulation consistent with the reference case study upon which this work is based.

1.3 Thermal effects and cooling

1.3.1 Heat exchange in transformers

The two principal sources of heat inside an operating transformer are the Joule (I^2R) losses in the winding conductors, which scale with the square of the load current and are therefore strongly load-dependent, and the no-load core losses, arising from hysteresis and eddy currents in the magnetic steel, which depend primarily on the applied voltage and frequency and are, to a first approximation, independent of load. Both heat sources must ultimately be conducted through the surrounding solid insulation to a surface in contact with the oil, from which they are removed by natural or forced convection, before finally being rejected to the ambient air (or, in some designs, to water) through an external heat exchanger: radiators in the simplest ONAN designs, or coolers equipped with fans and/or pumps in more heavily loaded machines.

Within the winding itself, the oil circulates through a network of axial and radial cooling ducts formed between the discs and between concentric winding layers. In the simplest, purely natural-convection arrangement, the buoyancy generated by the heating of the oil as it passes each disc drives a continuous circulation: oil enters at the bottom of the winding, is progressively heated as it rises past each successive disc, and exits at the top to be cooled externally before re-entering the winding at the bottom. The resulting flow distribution among the many parallel cooling ducts, and the resulting temperature distribution within the winding, are strongly coupled and are governed by a delicate balance between the buoyancy forces driving the flow and the hydraulic resistance of the duct network, a balance that is not, in general, uniform across the winding, giving rise to localised hot-spots that are of particular concern to the transformer designer, since the hottest point in the winding is what ultimately limits the rated load of the machine. Predicting the location and magnitude of this hot-spot temperature, for a specific winding geometry and cooling arrangement, is precisely the class of problem addressed by the computational fluid dynamics analysis presented in this thesis.

The heat-transfer process can be viewed as a sequence of coupled mechanisms. Heat generated inside the copper is first conducted through the solid conductor and its paper insulation, after which heat is transferred from the oil-wetted surface to the circulating oil by convection. For a convective boundary, the heat-transfer rate can be written as $\dot{Q} = hA(T_s - T_f)$, where h is the convective heat-transfer coefficient, A is the exchange area, and T_s and T_f are the solid-surface and adjacent-fluid temperatures, respectively. For one-dimensional conduction through an insulating layer, the corresponding thermal resistance is $R_{th} = L/(kA)$, giving $\Delta T = \dot{Q}R_{th}$. These relations provide a useful physical interpretation of the conjugate solution: the paper layer contributes a conduction resistance, while the oil-side flow determines the local convective resistance. Radiation is relevant mainly to heat rejection from the external transformer surfaces and is not part of the internal winding CHT domain modelled in this thesis.

1.3.2 Cooling arrangements

Cooling arrangements for oil-immersed transformers are conventionally identified by a four-letter code specifying, in order: the internal cooling medium, the mechanism of its circulation inside the winding, the external cooling medium, and the mechanism of its circulation outside the tank. The most relevant classes are:

- ONAN (Oil Natural, Air Natural), the oil circulates through the winding purely by natural convection, and the external radiators reject heat to the surrounding air, again by natural convection; the simplest and most reliable arrangement, and the one most directly relevant to the natural-convection winding model studied in this thesis.

- ONAF (Oil Natural, Air Forced), as ONAN, but with fans forcing air across the external radiators to increase the external heat transfer coefficient and hence the rated capacity of the same cooling surface.
- OFAF / ODAF (Oil Forced / Oil Directed, Air Forced), pumps are added to force (or, in directed-flow designs, specifically guide) the oil through the winding ducts, substantially increasing the achievable cooling capacity at the cost of additional auxiliary equipment, power consumption, and a further potential failure mode.

A single transformer may be designed to operate under more than one of these classes simultaneously, with pumps and fans switching on automatically as load increases, in order to combine the reliability of a naturally cooled base rating with an increased overload capacity when required.

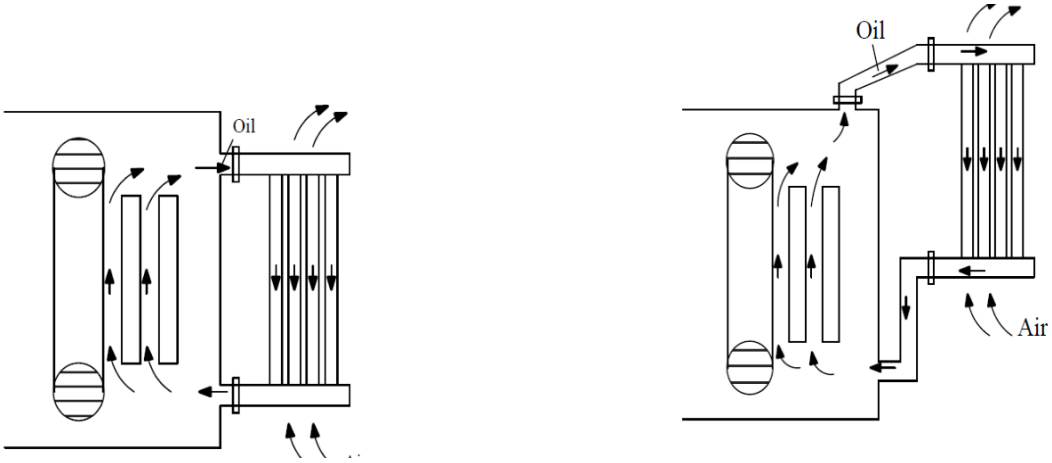


Figure 1.3: Schematic of ONAN cooling and ONAN with elevated radiators (adapted from Vezzani [7, Figs. 1.8–1.9]).

In an ONAN system, the internal oil circulation is driven by density differences produced by heating in the active region and cooling in the radiators. The resulting circulation therefore depends on the competition between the buoyancy head generated by the temperature difference and the hydraulic losses of the complete oil circuit. Raising the radiators increases the available buoyancy head and can increase the oil flow rate, but it also changes the hydraulic characteristics of the circuit. In ONAF systems, forced air increases the external heat-transfer coefficient, while OFAF systems additionally use a pump to increase the oil circulation rate. These distinctions provide the system-level context for the natural-convection winding flow model investigated in this thesis.

1.3.3 Ageing of insulation and operating life

The operating life of a power transformer is, in practice, governed by the rate of thermal ageing of its solid cellulose insulation rather than by the degradation of any other component. Cellulose ages through a combination of hydrolytic, oxidative and pyrolytic reactions that progressively reduce the degree of polymerisation of the paper fibres, and hence its mechanical strength; because these reactions are thermally activated, the rate of ageing approximately doubles for every 6–8 °C increase in the local hotspot temperature, a relationship generally attributed to the Montsinger rule and refined in international loading guides (IEC 60076-7, IEEE C57.91). This strongly nonlinear dependence on hotspot temperature is what makes accurate prediction of the winding's peak operating temperature, rather than merely its average temperature, the central design and analysis objective in transformer thermal engineering, and is the underlying motivation for the detailed, spatially resolved computational fluid dynamics analysis of the winding cooling ducts presented in the remainder of this thesis.

1.4 Thermal analysis

1.4.1 Analytical methods

The traditional approach to transformer thermal design relies on simplified analytical or empirical correlations relating the average and hotspot winding temperature rises to the total losses, the oil flow rate, and a small number of geometric parameters, calibrated against factory heat-run test data and codified in international loading guides such as IEC 60076-7 and IEEE C57.91. These methods are computationally inexpensive and remain in wide industrial use for routine design verification, but they provide only lumped, spatially averaged information and rely on empirical correction factors (such as the hotspot factor relating the calculated hotspot rise to the average winding rise) that must be calibrated for each winding type and cooling arrangement, and that do not, by construction, capture the detailed flow and temperature distribution within an individual winding pass.

1.4.2 Direct measurement

Direct temperature measurement, whether through embedded fibre-optic sensors during factory heat-run tests or, less commonly, through instrumented in-service monitoring, remains the ultimate validation route for any thermal design, and is indispensable for the calibration of both analytical and numerical models. Direct measurement is, however, expensive, is necessarily limited to a small number of discrete sensor locations that may not coincide with the true hotspot, and cannot easily be used to explore the effect of design variations without building and testing further physical prototypes, motivating the increasing recourse to numerical simulation, discussed next, as a complementary and considerably more flexible design tool.

1.4.3 Numerical methods

Numerical thermal-hydraulic modelling of transformer windings has developed along two broad lines. The first, historically the more widely used in industrial practice, treats the winding cooling-duct network as an equivalent hydraulic circuit and solves a reduced set of one-dimensional mass, momentum and energy balance equations for the flow rate and temperature rise in each duct, the so-called thermal-hydraulic network (THNM) approach. These models are computationally efficient enough to be used routinely in design iteration, but rely on empirical friction-factor and heat-transfer correlations for the flow within a duct, and cannot resolve the genuinely two- or three-dimensional flow structures (recirculation, flow reversal, local separation) that can occur within individual ducts, particularly under natural-convection conditions where the driving pressure differences are small and the flow is correspondingly sensitive to local geometric detail.

The second line of development, and the one adopted in this thesis, applies full computational fluid dynamics (CFD) to the winding cooling ducts, solving the Navier–Stokes and energy equations directly (or, for turbulent regimes, in Reynolds-averaged form) over a spatially resolved computational mesh of the duct geometry, typically coupled to a conduction solution in the solid conductor and insulation regions to form a conjugate heat transfer problem. This approach is considerably more computationally demanding than a network model, but removes the need for empirical duct-level correlations and can directly resolve the local flow and temperature fields, including the hotspot location and magnitude from first principles. The steady growth in affordable computing power, together with the maturation of open-source CFD toolkits such as OpenFOAM, has made this approach increasingly attractive for detailed academic and industrial studies of individual winding passes, and is the approach pursued throughout the remainder of this thesis, building directly on the methodology established in Torriano et al. and in the more recent work of Salerno et al. on this same class of disc-type winding geometry.

1.5 Dimensionless groups in natural-convection cooling

The buoyancy-driven flow within a transformer winding's cooling ducts is conventionally characterised by three dimensionless groups, each of which recurs throughout the numerical results discussed in the following chapters. The Grashof number,

$$Gr = g\,\beta\,\Delta T\,L^3 / \nu^2$$

compares the buoyancy force driving the flow to the viscous force resisting it, where ΔT is a characteristic temperature difference, L a characteristic length scale (here, the duct width or the disc height, depending on the direction of interest), and ν the kinematic viscosity of the oil. The Prandtl number,

$$Pr = \nu / \alpha = \mu\,Cp / k$$

compares the fluid's momentum diffusivity to its thermal diffusivity α, and is a fluid property alone, independent of the flow or geometry; the transformer oil considered in this thesis has a comparatively high Prandtl number, of order 100, reflecting mineral oil's much higher viscosity relative to its thermal diffusivity when compared with, say, water or air. The product of the Grashof and Prandtl numbers gives the Rayleigh number,

$$Ra = Gr \cdot Pr$$

which is the single dimensionless group most commonly used to characterise the onset and vigour of natural-convection flow and, in particular, the transition from a stable, stratified flow to an unstable, oscillatory or cellular one; the classical Rayleigh–Bénard instability, in which a horizontal fluid layer heated from below becomes unstable above a critical Rayleigh number of approximately 1708 for idealised conditions, is frequently invoked, including in the Task 2 discussion of Chapter 5, as a qualitative explanation for the oscillatory, cellular flow structures observed in this winding's narrow cooling ducts under certain conditions, and is associated in the literature on this exact geometry with locally reduced Prandtl numbers below approximately 100.

These three dimensionless groups do not appear explicitly as inputs to the CFD solver, which instead solves the dimensional governing equations of Section 2.2 directly; they are nonetheless a useful lens through which to interpret the resulting flow fields, and in particular to understand why a winding cooling duct, however narrow and however small the driving temperature difference across it, can nonetheless sustain a genuinely unsteady or oscillatory flow rather than settling into the smooth, laminar, single-direction circulation that a purely geometric or thermal-resistance-based argument might suggest.

Chapter 2

Case Study

2.1 Description of the geometry

The case study adopted throughout this thesis reproduces the low-voltage, disc-type winding of an oil-immersed power transformer investigated by Torriano and, more recently, by Salerno et al., and is modelled as a two-dimensional axisymmetric wedge in order to keep the computational cost of the study tractable while retaining the essential physics of the buoyancy-driven flow within a single winding pass. A full winding pass consists of nineteen paper-wrapped copper discs, arranged as flat, radially extended conductors stacked in the axial direction and separated from one another by twenty axial cooling ducts through which the oil circulates; a two-disc entry region precedes the main stack of discs, reproducing the geometry of the physical winding's oil inlet. Each copper disc is individually wrapped in a layer of kraft paper insulation, explicitly resolved as a separate solid region in the computational model rather than lumped into an equivalent thermal resistance, so that the conduction path from the heat-generating copper through the paper to the oil-wetted surface is captured directly.

The oil-filled fluid domain spans x = 0.316007–0.383466 m in the radial direction and y = −0.4134–0 m in the axial direction (coarse-mesh bounding box), with the inner cooling channel located at x ≈ 0.317 m and the outer cooling channel at x ≈ 0.380 m. The true winding is, of course, axisymmetric about the transformer's central axis; because the winding radius is very large compared with the radial extent of a single pass, the curvature of the winding can be neglected without materially affecting the local flow and temperature field, and the domain is instead modelled as a thin, quasi-planar axisymmetric wedge of approximately 1° angle, discretised with a single layer of cells in the circumferential (wedge) direction and bounded by OpenFOAM's dedicated wedge boundary condition on the two circumferential faces. This device allows a fully three-dimensional solution of the governing equations to be obtained at essentially the computational cost of a two-dimensional simulation.

The two-pass extension of the model considered in Chapter 5 retains the same disc, duct and insulation geometry, replicated over two winding passes separated by a radial gap through which the oil transfers from the first to the second pass, in place of the single-pass domain described above.

2.2 Governing equations

The oil flow is treated as laminar, incompressible (or weakly compressible, in the sense of the Boussinesq or variable-property models discussed below) and buoyancy-driven, governed by the steady-state continuity, momentum and energy equations:

$$\nabla \cdot u = 0$$

$$\rho\,(u \cdot \nabla)\,u = -\nabla p + \mu\,\nabla^2 u + \rho\, g\, \beta\,(T - T_{ref})$$

$$\rho\, Cp\,(u \cdot \nabla)\,T = \nabla \cdot (k\,\nabla T)$$

where u is the velocity field, p the pressure, ρ the density, μ the dynamic viscosity, g the gravitational acceleration, β the thermal expansion coefficient, T the temperature, Tref a reference temperature, Cp the specific heat and k the thermal conductivity of the oil. In the copper and paper solid regions, the corresponding steady conduction equation $\nabla \cdot (k\,\nabla T) = 0$ is solved, augmented by a uniform volumetric heat source term in the copper region representing the Joule losses of the conductor; the two solid regions and the fluid region are coupled at their shared interfaces through matched temperature and heat-flux

boundary conditions, forming a conjugate heat transfer (CHT) problem solved simultaneously (in a segregated, iterative sense) across all three regions.

Two distinct closure models for the oil's buoyancy term and thermophysical properties are used in this thesis, corresponding to Task 1 (Chapter 4) and Task 2 (Chapter 5) respectively. In Task 1, and in the Boussinesq variant of Task 2, the oil is treated as having constant thermophysical properties throughout the domain, with the buoyancy force alone retaining a temperature dependence through the linearised Boussinesq approximation shown in the momentum equation above. In the variable-properties variant of Task 2, the oil's density, viscosity, thermal conductivity and specific heat are instead evaluated locally as polynomial functions of temperature, following the correlations reported by Torriano, providing a more physically complete, but also more numerically demanding, representation of the flow, against which the validity of the simpler Boussinesq approximation can be assessed (Section 5.2 and Section 5.4).

2.3 Boundary and operating conditions

The oil enters the fluid domain at the bottom inlet of the entry region with a uniform velocity U = (0, 0.027, 0) m s^{-1}, directed axially upward, and a uniform temperature T = 319.85 K; a fixed-value condition (p_rgh = 0 for task1 both coarse and refin mesh, but for task 2 it is set as 1e5 Pa) is imposed at the domain outlet, at the top of the winding stack. Gravity acts in the negative axial (y) direction, g = (0, −9.81, 0) m s^{-2}, driving the buoyant recirculation within and between the cooling ducts. On the wedge's circumferential faces, the dedicated OpenFOAM wedge boundary condition is applied to all fields, enforcing the axisymmetric character of the solution; the outer radial boundary of the domain is treated as adiabatic and impermeable, consistent with its physical role as a symmetry-like boundary between adjacent, thermally similar sections of the same winding.

The volumetric heat source applied within the copper region is set such that the total dissipated power over the whole modelled pass equals 157.943 W, matching the value used in the original reference case and corresponding to the rated Joule losses of the low-voltage winding of the physical transformer under the operating condition considered. A summary of the thermophysical properties used for the oil, copper and paper regions in the constant-property Task 1 model is given in Table 2.1 (the copper and paper values carry over unchanged to Task 2); the variable-property correlations used for the oil in the Task 2 variable-properties model are given separately in Section 5.1, and the separate, hotter reference state used for the Task 2 Boussinesq model is given in Section 5.3.2.

Region	ρ [kg/m³]	Cp [J/(kg·K)]	k [W/(m·K)]	Other parameters
Oil	870.99	1952.23	0.128	$\nu = 9.05\times10^{-6}$ m²/s, $\beta = 8.18\times10^{-4}$ K⁻¹, Pr = 120, Tref = 319.85 K
Copper	8933	385	401	Total heat source $\dot{R}$ = 157.943 W / ~300 W
Paper	930	1340	0.19	N/A

Table 2.1: *Constant thermophysical properties adopted for the oil, copper and paper regions for Task 1 (copper and paper values also apply to Task 2; see Section 5.3.2 for the separate Task 2 Boussinesq reference state).*

2.4 Mesh independence considerations

Because a natural-convection flow in a narrow duct can be sensitive to the local near-wall resolution, an under-resolved boundary layer can artificially damp or, conversely, artificially destabilise the buoyant

recirculation, every simulation reported in this thesis was carried out on at least two mesh densities, a coarse mesh and a refined mesh, with cell counts differing by a factor of approximately four in the solid regions and a comparable factor in the fluid region (Section 4.6). This follows the same practice adopted in the reference literature (Torriano; Salerno et al.), which likewise reports that no dedicated formal mesh-independence (e.g. Richardson extrapolation) study was carried out, the mesh density instead being fixed at values previously established as adequate in that earlier work; the present thesis follows the same convention, using the coarse/refined comparison primarily as a check that the qualitative flow and temperature structure, and in particular the location and approximate magnitude of the winding hot-spot, are not artefacts of the coarser of the two meshes, rather than as a rigorous asymptotic-convergence exercise.

A structured, purely hexahedral cell topology was used throughout, in both the fluid and solid regions, in preference to an unstructured or hybrid mesh, in order to keep the total cell count, and hence the computational cost of running four to six independent simulations per task, several of them for many thousands of iterations, within a range tractable on a single workstation over the timescale of this thesis. The solid regions (copper and paper) use the same uniform cell spacing in both the radial and axial directions, without near-interface refinement, since heat transport within a solid conductor and its insulation occurs purely by conduction and there is, in the classical sense, no boundary layer to resolve there; the fluid region, in contrast, is refined toward the duct walls to resolve the momentum and thermal boundary layers that govern the convective heat transfer coefficient.

Chapter 3

Numerical Methodology

3.1 Mesh generation workflow

All computational meshes used in this thesis, coarse and refined single-pass meshes (Chapter 4) and the two-pass mesh (Chapter 5), were built using the commercial mesh generator Pointwise, with a fully structured, hexahedral block topology chosen throughout in order to keep the total cell count manageable while still resolving the thin thermal and momentum boundary layers that develop along the duct walls and along the copper–paper and paper–oil interfaces. Because the flow is dominated by natural convection at modest driving temperature differences, adequate near-wall resolution is essential to correctly capture the buoyant boundary layer and, ultimately, the winding's hotspot temperature.

A specific methodological point deserves explicit mention, since it was the source of a protracted debugging effort during this work and is likely to recur for anyone repeating this procedure with Pointwise and OpenFOAM: Pointwise's CAE export does not natively produce the angled axisymmetric wedge mesh required by OpenFOAM's wedge boundary condition. A mesh exported directly with a non-zero wedge angle passes Pointwise's own internal checks but subsequently fails OpenFOAM's checkMesh with a very large number of under-determined ('zero or negative determinant') cells, in the case of this geometry, on the order of 370 000 flagged cells, essentially the entire domain. The correct procedure, eventually identified from an internal project note documenting an earlier, successful attempt at the same class of mesh, is instead to export a flat, purely two-dimensional mesh from Pointwise and to add the wedge angle afterward, on the OpenFOAM side, using the extrudeMesh utility with a wedge extrusion model. Table 3.1 summarises this recipe, which was applied, unchanged in its logical structure, to the coarse, refined and two-pass meshes described in Chapters 4 and 5.

Step	Operation
1	Export a flat, two-dimensional mesh from Pointwise, in millimetres.
2	Extrude the mesh through a thin wedge angle (~1–2° total, i.e. ~0.5–1° per side) using OpenFOAM's extrudeMesh utility with the wedge extrusion model, a single cell layer, and the correct axis point and axis direction for the winding's true axis of revolution.
3	Verify with checkMesh -allTopology -allGeometry; a genuinely correct wedge extrusion returns “Mesh OK” with the cell-determinant check passing, the definitive confirmation that the earlier direct-export approach was actually failing on.
4	Split the single extruded mesh into fluid (oil), copper and paper regions using splitMeshRegions -cellZonesOnly, based on cellZones assigned during the Pointwise export; every cell must belong to exactly one cellZone or the utility fails outright.
5	Convert the mesh from millimetres to metres with transformPoints -scale "(0.001 0.001 0.001)", applied to each region.
6	Renumber each region's mesh with renumberMesh -overwrite for solver efficiency.
7	Repeat the checkMesh -allTopology -allGeometry verification on each individual region as a final confirmation.

Table 3.1: *Mesh-generation and verification workflow applied to every mesh used in this thesis.*

An earlier, ultimately discarded meshing route, in which the flat OpenFOAM-native mesh was instead built up by trimming, translating and merging separate sub-meshes with coupled mapped boundary conditions at their shared interface, was found to pass all standard geometric quality checks but to contain a subtle, slowly accumulating mass-conservation defect localised at the internal junction between sub-meshes; long-duration runs on this mesh diverged after an extended but clean-looking transient. The single, genuinely continuous conformal mesh produced by the extrudeMesh-based recipe of Table 3.1 removes this junction entirely and was adopted for all mesh-dependent results reported in this thesis.

3.2 Solver and discretisation schemes

All simulations in this thesis were carried out with OpenFOAM v2306, using the multi-region, steady-state, segregated SIMPLE-algorithm conjugate heat transfer solver chtMultiRegionSimpleFoam, which solves the flow and energy equations in the fluid region and the conduction equation in each solid region within a single outer iteration loop, exchanging boundary temperature and heat-flux information at each coupled interface until the whole multi-region system reaches a converged steady state.

The momentum and enthalpy equations are solved with the PBiCGStab solver and a DILU preconditioner (absolute tolerance 10^{-6}, relative tolerance 0.1 within each outer iteration, under-relaxation factor 0.3). The pressure (p_rgh) equation is solved with a PCG solver and a DIC preconditioner (absolute tolerance 10^{-8}, relative tolerance 0.01, under-relaxation factor 0.3); a GAMG multigrid solver, the more commonly recommended choice for the pressure equation in OpenFOAM, was tested first but was found to diverge with a floating-point exception essentially immediately from a cold start on this mesh topology, and PCG was adopted in its place for all runs reported in this thesis. The SIMPLE algorithm's momentum predictor step is retained (enabled), and the explicit non-orthogonal correction term div((rho*nuEff)*dev2(T(grad(U)))) in the momentum equation (sometimes omitted for computational economy on well-behaved meshes) was found to be required for a numerically stable solution on the disc-type winding geometry studied here.

Time-stepping controls follow OpenFOAM's standard steady-state pseudo-transient practice: a write interval of 10 iterations with purgeWrite set to retain only the most recent 5 written time directories (to limit disk usage over runs extending to several thousand iterations), runTimeModifiable enabled so that solver controls could be adjusted without restarting a run, and, critically, startFrom set to latestTime rather than startTime: an OpenFOAM v2306 multi-region case with startFrom startTime was found to silently restart from the initial (zero) fields rather than resuming from the most recent written time directory, a behaviour that is not immediately obvious from the solver log and that, if unnoticed, would invalidate any attempt to resume a partially converged run.

3.3 Validation reference

The original, pre-existing implementation of the single-pass model, against which the OpenFOAM port is validated in Chapter 4, was built with the solver conjugateHeatSimpleFoam in foam-extend 4.0, an independently maintained fork of OpenFOAM with its own solver architecture and, in particular, its own pressure–velocity coupling normalisation, meaning that the raw magnitude of p_rgh is not directly comparable between the two codes even where the underlying physical pressure field is essentially identical; temperature and velocity, in contrast, are directly comparable. The foam-extend case represents fluid and solid regions with a single hardcoded region0 (fluid) plus a solid region internally subdivided by cellZones (copper-cells, paper-cells), a somewhat different region topology from the three explicitly split regions (oil, copper, paper) used in the OpenFOAM port, requiring some care in translating boundary condition and field specifications between the two during the porting exercise documented in Chapter 4. Both foam-extend reference cases used in this thesis (coarse and refined mesh) were run to full convergence, with residuals at or below machine precision (of order 10^{-13}–10^{-14}) and a negligible

cumulative continuity error, and are treated throughout as the ground truth against which the ported OpenFOAM solution is assessed.

3.4 Discretisation schemes

Table 3.2 summarises the finite-volume discretisation schemes used for the principal terms of the governing equations, common to all simulations reported in this thesis unless otherwise noted in Chapter 5 for the variable-properties model. Second-order schemes are used throughout for the gradient, divergence and Laplacian terms, consistent with the intent of obtaining a spatially accurate steady-state solution rather than merely a qualitatively plausible one; a bounded, upwind-biased divergence scheme (linearUpwind, or an equivalent limited-linear scheme) is used for the momentum and energy convection terms to maintain numerical stability in regions of locally reversed or recirculating flow, of which there are many in this problem, as discussed in Chapter 4.

Term	Scheme
Gradient, ∇	Gauss linear (second-order, unbounded)
Divergence, $\nabla\cdot(U\,U)$, $\nabla\cdot(U\,h)$	Gauss linearUpwind grad(U) / grad(h) (second-order, bounded)
Laplacian, ∇^2	Gauss linear corrected (second-order, with explicit non-orthogonal correction)
Time derivative	steadyState (pseudo-transient SIMPLE iteration, Section 3.2)
Interpolation	linear
Surface-normal gradient	corrected

Table 3.2: *Finite-volume discretisation schemes used for the principal terms of the governing equations.*

Non-orthogonal mesh correction was found to be necessary, rather than merely beneficial, for a stable solution on the structured but locally skewed mesh produced by the wedge-extrusion procedure of Section 3.1, particularly in the transition regions between the entry ducts and the main disc stack; simulations run with the simpler, uncorrected Laplacian scheme exhibited spurious pressure oscillations that propagated and amplified rather than remaining bounded.

3.5 Verification metrics

Two complementary metrics are used throughout this thesis to assess the convergence of a given simulation. The first is the standard OpenFOAM solver residual, computed and reported separately for each solved field (Ux, Uy, p_rgh, h in the fluid region; T in each solid region) at every outer iteration, and interpreted in the usual way: a residual that decreases monotonically, or that has decreased by several orders of magnitude from its initial value and settled into a small, bounded oscillation, is taken as evidence of convergence for that individual field.

The second, and in several respects the more informative metric for this specific class of problem, is the cumulative continuity error reported by OpenFOAM's pressure solver at each outer iteration, an integral measure of the net mass imbalance accumulated over the course of the run. Because the coarse-mesh Task 1 case (Section 4.2.1) and several of the Task 2 cases (Chapter 5) settle into a bounded p_rgh oscillation

rather than a monotonically vanishing residual, the trend of the cumulative continuity error over an extended run (specifically, whether it is tightening toward a stable value, oscillating within a fixed narrow band, or drifting without bound) is used throughout this thesis as the primary discriminator between an acceptable, physically bounded numerical oscillation and a genuine divergence, a distinction that a snapshot of the instantaneous residuals alone cannot reliably make.

3.6 Practical implementation lessons

A number of practical, and in several cases non-obvious, implementation issues were encountered and resolved over the course of this work. They are recorded here in some detail, both because they materially affected the time and effort required to obtain the results reported in Chapters 4 and 5, and because they are likely to be directly useful to anyone repeating or extending this class of multi-region conjugate heat transfer simulation in OpenFOAM.

3.6.1 Region-splitting and coupled-interface consistency

Splitting a single mesh into several regions with splitMeshRegions requires the -cellZonesOnly option. Using the more general -cellZones option can split the mesh into many separate regions instead of the intended three regions: oil, copper, and paper. In an early attempt, this produced around 400 disconnected regions because separate disconnected groups of cells were treated as different regions.

Another important requirement is that every cell must belong to exactly one cellZone. If even a small number of cells are left unassigned, splitMeshRegions stops without producing a partial result. In one case, 748 cells near an outlet corner were not assigned to any zone. These cells were identified using topoSet, by subtracting the correctly assigned zones from a selection covering the whole mesh. Their location was then checked with foamToVTK and ParaView before assigning them to the correct region.

After the mesh is split, boundary conditions that refer to another region by name must also be updated consistently. This is particularly important for entries such as sampleRegion in mapped boundary conditions. If the region names are changed but the corresponding boundary conditions are not updated on both sides, the solver may not crash but the interface coupling can become incorrect.

3.6.2 Mesh-quality verification

A standard checkMesh command without additional options does not perform all of the checks needed for this type of wedge mesh. In particular, it does not check the cell determinant or fully verify the wedge geometry. The wedge-angle check is also only performed when the corresponding boundary is correctly defined as a wedge patch. For this reason, checkMesh -allTopology -allGeometry was used for the final mesh verification. The cell-determinant check was especially useful for identifying the difference between a correctly constructed wedge mesh and the apparently valid but malformed meshes produced when the wedge angle was exported directly from Pointwise. A warning about **“multiply connected (shared edge)”** was also observed on some of the automatically generated internal faces between regions. After checking the mesh topology, this was found to be a normal consequence of the multi-region mesh structure and not an actual mesh-quality problem.

3.6.3 Solver-specific requirements

Several solver-specific issues were identified during the implementation. These were not obvious from the OpenFOAM documentation and only became clear while setting up and running the cases.

The first issue concerned the copper and paper regions, which use the rhoConst thermodynamic model with chtMultiRegionSimpleFoam. Although pressure has no physical role in a solid conduction region, the solver still requires a p field to be present in the region's initial-conditions directory. When this field is missing, the solver simply stops during start-up without clearly indicating that the pressure field is the cause. For this reason, a placeholder p field must be included in the solid regions even though it is not used physically.

The second issue was related to the createPatch utility. It was found that when the requested patch name already exists in the mesh, createPatch may ignore the requested change without producing an error or warning. The mesh therefore remains unchanged, which can be difficult to notice. To avoid this problem, a new and previously unused patch name should be used whenever createPatch is required to change a boundary type.

The third issue involved the postProcess -func utility, which was used in Chapter 4 to extract the line-sample data for comparison. The function-object dictionary must be written as a simple top-level dictionary, without comments or an additional enclosing sub-dictionary. Some OpenFOAM tutorial cases use a nested structure, but copying that structure directly can cause postProcess -func to treat the dictionary as empty. The resulting error only reports that an entry was not found, which makes the problem appear to be related to the function-object content when the actual issue is the structure of the dictionary.

Chapter 4

Porting and Validation of the Single-Pass Model (Task 1)

4.1 Objectives

This chapter presents the porting of the single-pass, two-dimensional conjugate heat transfer model described in Chapter 2 from foam-extend 4.0 to OpenFOAM v2306, together with its validation against the original foam-extend results using both coarse and refined meshes. The main goals are to reproduce the original temperature distribution in the oil, copper, and paper regions, as well as the buoyancy-driven flow in the cooling ducts, using a currently maintained open-source solver. The study also aims to distinguish actual physical or numerical differences between the two solvers from differences caused by their different solver implementations.

The coarse mesh was studied first because its lower computational cost made it easier to establish and refine the numerical setup. The boundary conditions, thermophysical properties, discretisation schemes, and solver settings described in Chapter 3 were tested on the coarse mesh before being applied to the refined mesh in Section 4.6. The common mesh-generation procedure is described in Section 3.1, while this chapter focuses on the mesh sizes, convergence behaviour, and validation results.

Both meshes were compared with the foam-extend reference. The coarse-mesh simulation was run to full convergence, so the comparison presented in Section 4.4 provides a direct validation between the two solvers. The refined-mesh simulation, however, was stopped before reaching convergence. Its results in Section 4.6.2 are therefore presented as an early-transient comparison with the converged foam-extend solution. They are mainly used to confirm that the refined mesh and simulation setup are working correctly, rather than as a final accuracy comparison between the two meshes.

4.2 Coarse mesh

The coarse mesh consists of 189 301 cells in the oil region, 97 650 cells in the copper region and 83 916 cells in the paper region, for a total of 370 867 hexahedral cells, generated according to the workflow of Section 3.1.

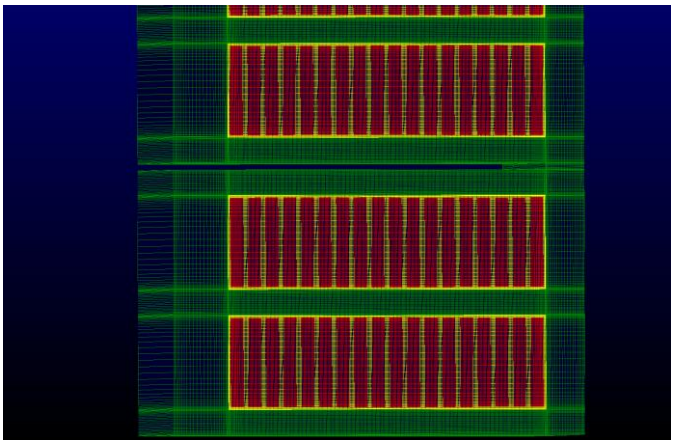


Figure 4.1: *Detail of the structured block topology around adjacent discs: copper conductors (red), paper wrap (yellow) and oil ducts (green).*

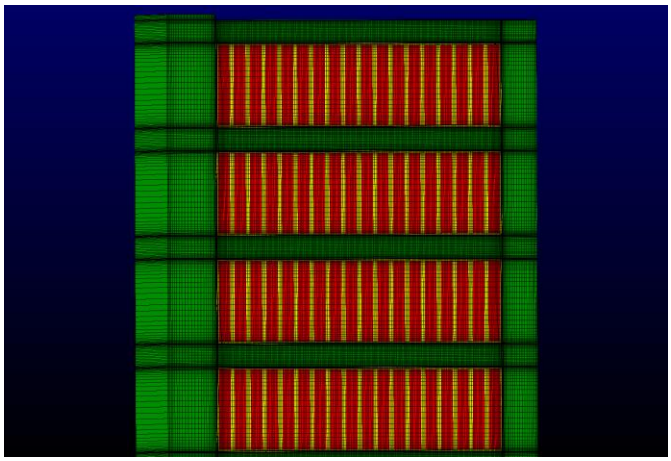


Figure 4.2: *Further detail of the mesh grading within discs and adjacent cooling ducts.*

4.2.1 Convergence history

The coarse-mesh case was run till final iteration, $t = 947\,067$. The cumulative continuity error crossed zero at around $t = 50\,001$and then settled at approximately 0.275 for the rest of the run, indicating stable mass conservation. Over the same period, the oil temperature range increased gradually at the upper end, from 319.85–330.64 K at $t = 50\,001$to 319.85–365.29 K at the final iteration. This increase reflects the gradual heating of the oil as the solid regions continued to reach thermal equilibrium. The lower temperature remained close to the inlet value of 319.85 K throughout the run. Together, these results indicate that the solution reached a stable steady state. The final state at $t = 947\,067$was therefore used for the quantitative comparison with the foam-extend reference in Section 4.4.

4.3 Sampling methodology

Quantitative comparison between the OpenFOAM and foam-extend results was carried out along five sampling lines using the same spatial locations in both cases:

- **Inner channel:** a vertical line at $x = 0.317$m, from $y = -0.4134$m to $y = 0$, sampling temperature T, velocity U, and p_{rgh} in the oil.
- **Outer channel:** a vertical line at $x = 0.380$m, using the same sampling fields.
- **Horizontal line:** a line at $y = -0.20$m spanning the radial extent of the domain and restricted to the oil region.
- **Copper line:** the same horizontal location at $y = -0.20$m, covering $x = 0.3249$–0.3771 m and restricted to the copper region. Only temperature was sampled.
- **Paper line:** the same horizontal line, restricted to the paper regions and also sampling temperature only.

Because the OpenFOAM and foam-extend cases use different meshes, the sampling points are not exactly at the same coordinates. To make a proper comparison, each OpenFOAM point was matched with the nearest foam-extend point rather than comparing the data row by row. The coordinate differences were smaller than the local cell spacing, so this approach avoided errors caused by the two sets of points having slightly different positions.

The copper and paper samples form complementary parts of the same horizontal line because the copper discs are individually wrapped with paper. They therefore represent alternating sections of the same sampling line rather than two separate continuous regions.

The OpenFOAM field values were obtained by exporting the converged solution to VTK using foamToVTK. For each sampling point, the corresponding mesh cell was located using vtkCellLocator, and the field value was then calculated from the cell's nodal values using the interpolation weights provided by VTK's EvaluatePosition routine. This manual method was used because the standard VTK probe filter was found to be unreliable for the thin axisymmetric wedge mesh. The same procedure was used for the coarse- and refined-mesh samples and for the field-contour results presented in Sections 4.5 and 4.7.

4.4 Coarse-mesh quantitative comparison with the foam-extend reference

4.4.1 Fluid region

Figures 4.3–4.5 compare the temperature and velocity-magnitude profiles from OpenFOAM v2306 at the final converged state, $t = 947\,067$, with the fully converged foam-extend 4.0 reference. The comparison is shown along the inner-channel, outer-channel, and horizontal sampling lines. The foam-extend results were converged to residuals of approximately 10^{-13}–10^{-14}.

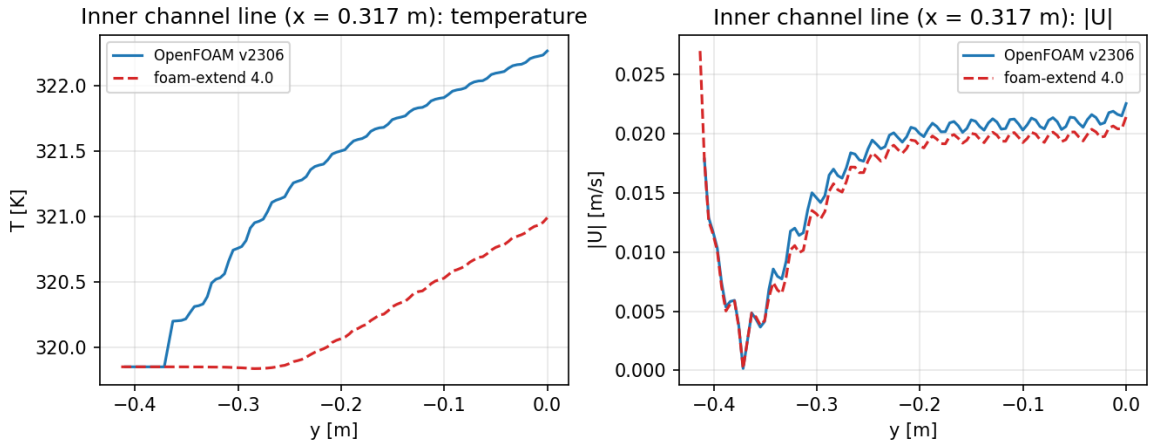


Figure 4.3: *Temperature and velocity-magnitude profiles along the inner channel line (x = 0.317 m), coarse mesh.*

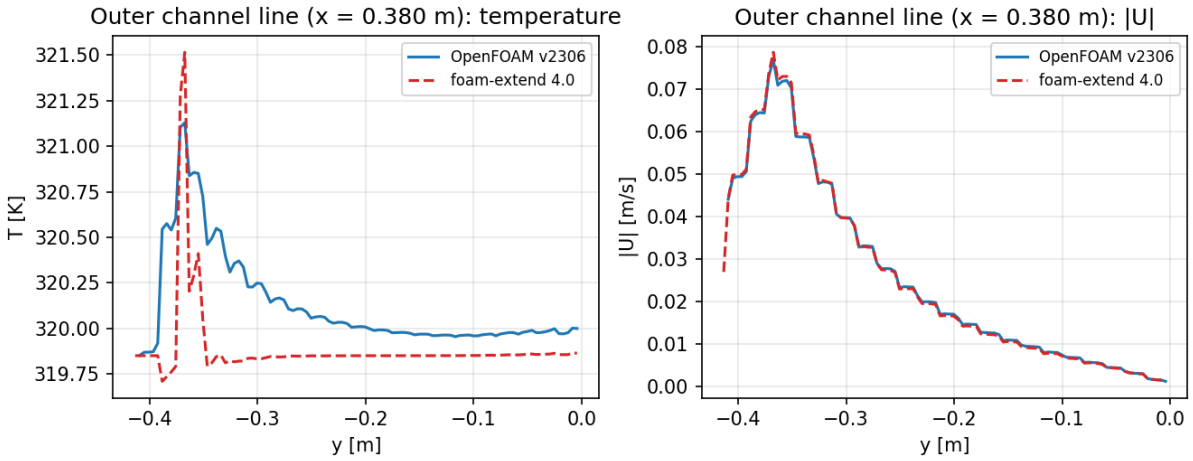


Figure 4.4: *Temperature and velocity-magnitude profiles along the outer channel line (x = 0.380 m), coarse mesh.*

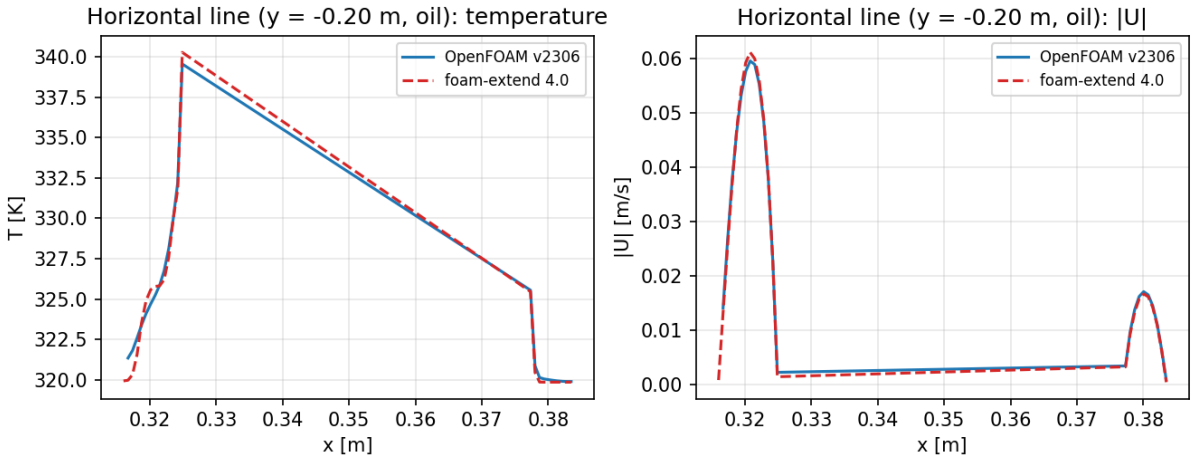


Figure 4.5: *Temperature and velocity-magnitude profiles along the horizontal line (y = −0.20 m, oil region), coarse mesh.*

The fluid-region temperature results agree very well along all three sampling lines. The mean absolute deviations are 1.08 K for the inner channel, 0.25 K for the outer channel, and 0.44 K for the horizontal line. In all three cases, both solvers reproduce the same overall temperature distribution.

The horizontal line has a slightly larger maximum deviation of 1.49 K, compared with 1.45 K for the outer channel and 0.84 K for the inner channel. This difference comes from a small number of points close to the fluid–solid interface, where the sampling line passes near a duct wall. Away from this region, the two solutions show very close agreement.

4.4.2 Solid regions

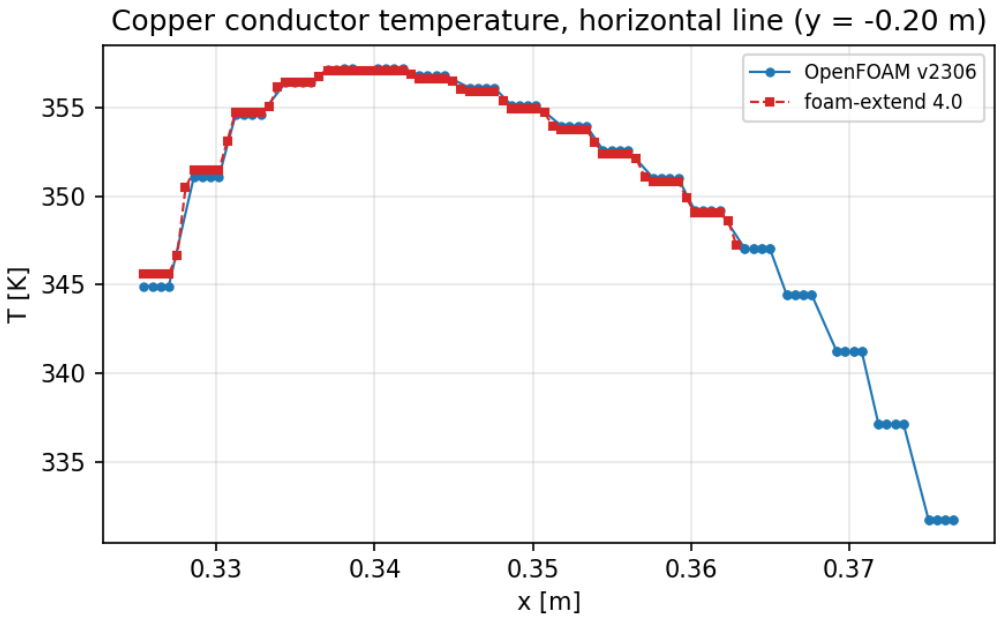


Figure 4.6: *Copper conductor temperature along the horizontal sampling line (y = −0.20 m), coarse mesh.*

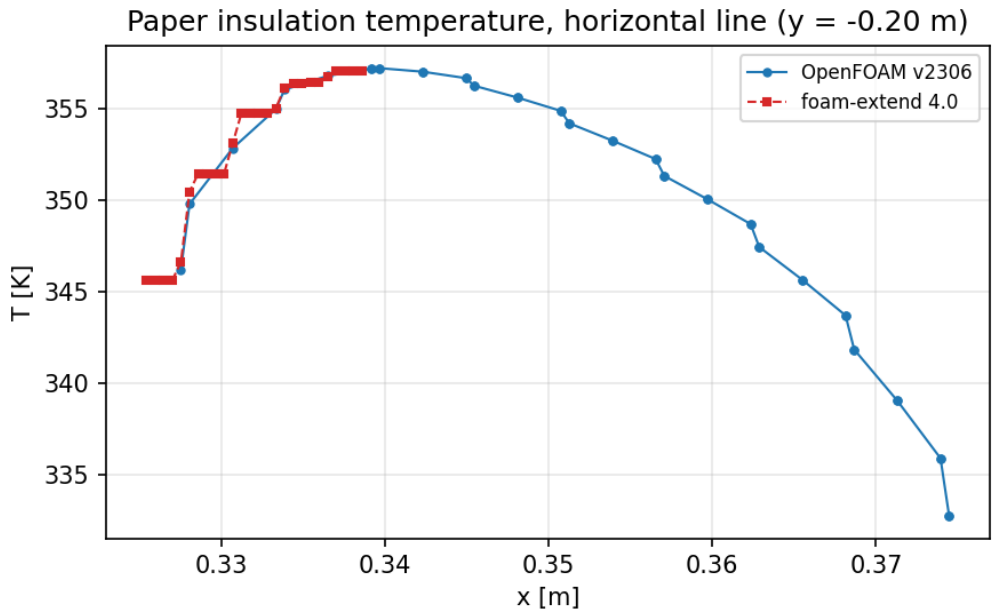


Figure 4.7: *Paper insulation temperature along the horizontal sampling line (y = −0.20 m), coarse mesh.*

The solid regions show a smaller, but still noticeable, difference. The mean absolute deviation is 4.28 K in the copper and 7.64 K in the paper. In both cases, the foam-extend results are consistently hotter than the OpenFOAM results, with maximum differences of 17.32 K in the copper and 24.32 K in the paper. These larger differences are mainly found near the centre of the discs, where the temperature gradient is strongest.

The difference is not due to the heat source. The volumetric heat generation was checked against the original value of 157.943 W and confirmed to be correctly applied to all copper cells. Instead, the difference

is mainly related to the slower heating of the solid regions compared with the fluid. The solids have a larger thermal mass and therefore take longer to reach their final temperature.

Despite the temperature difference, the copper and paper profiles follow the same overall shape as the foam-extend results. The hotspot location and the general temperature gradient across the discs are also reproduced correctly. This indicates that the OpenFOAM solution is still moving toward the same steady-state behaviour rather than showing a physical or setup error.

4.4.3 Summary

Sample line	OF mean [K]	FE mean [K]	OF range [K]	FE range [K]	Mean |ΔT| [K]	Max |ΔT| [K]
Inner channel	321.29	320.20	319.85–322.27	319.84–320.99	1.08	1.45
Outer channel	320.13	319.89	319.85–321.13	319.71–321.52	0.25	0.84
Horizontal (oil)	323.99	323.82	319.89–339.55	319.85–340.27	0.44	1.49
Copper (solid)	349.89	353.50	331.72–357.24	345.63–357.08	4.28	17.32
Paper (solid)	350.31	353.06	332.76–357.23	345.63–357.08	7.64	24.32

Table 4.1: *Summary of the coarse-mesh quantitative comparison between OpenFOAM v2306 (t = 947 067) and the foam-extend 4.0 reference.*

4.5 Field-contour visualisation, coarse mesh

Figures 4.8–4.9 show the temperature T, and velocity magnitude $|U|$. The results were obtained from the coarse mesh at the final converged state, $t = 947\,067$. The contours were generated from the exported VTK point data using Delaunay triangulation, with an edge-length filter applied to prevent non-physical triangles from forming across the gaps between the ducts and disc regions

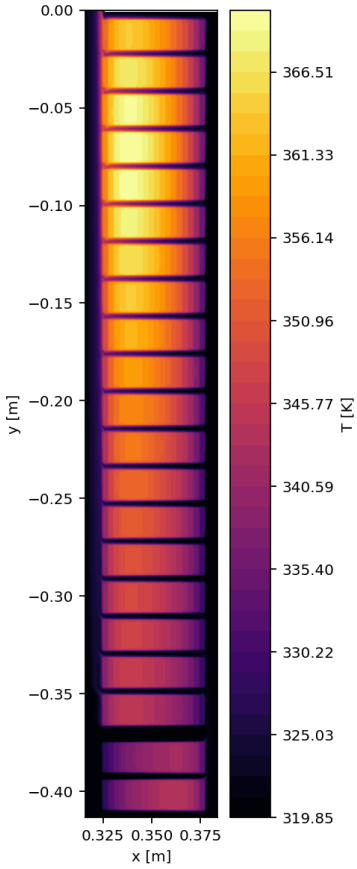


Figure 4.8: *Temperature field T on the coarse mesh.*

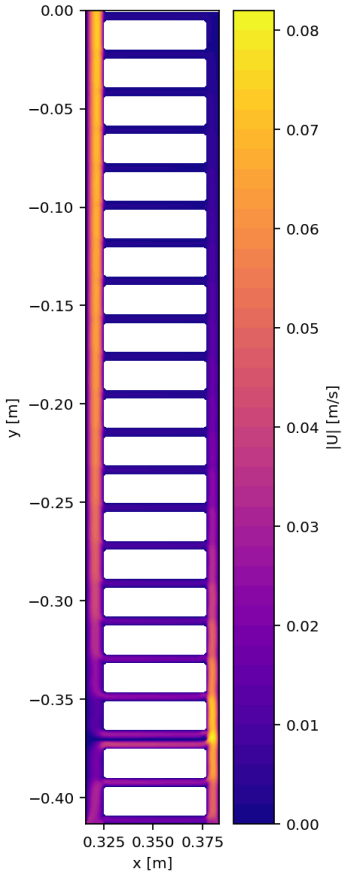


Figure 4.9: *Velocity-magnitude field |U| on the coarse mesh.*

The temperature field shows a clear hotspot near the top of the disc stack, while the oil in the narrow ducts between the discs remains cooler. This is consistent with the upward movement of the heated oil, which carries heat from the lower discs toward the outlet.

The velocity-magnitude field clearly shows the inner and outer axial ducts and the radial channels connecting the discs. The solid disc regions are correctly excluded from the oil contour, confirming that the flow field is being displayed only within the fluid region.

4.6 Refined mesh

The refined mesh uses the same block topology and boundary conditions as the coarse mesh described in Sections 4.2 and 3.1, but with a higher cell density to examine the effect of spatial discretisation. It contains 773,490 cells in the oil region, 407,400 cells in the copper region, and 341,040 cells in the paper region, giving a total of 1,521,930 cells. Compared with the coarse mesh, this corresponds to approximately 4.09 times more oil cells, 4.17 times more copper cells, and 4.06 times more paper cells. The refinement is therefore approximately uniform at four times the cell counts across all three regions.

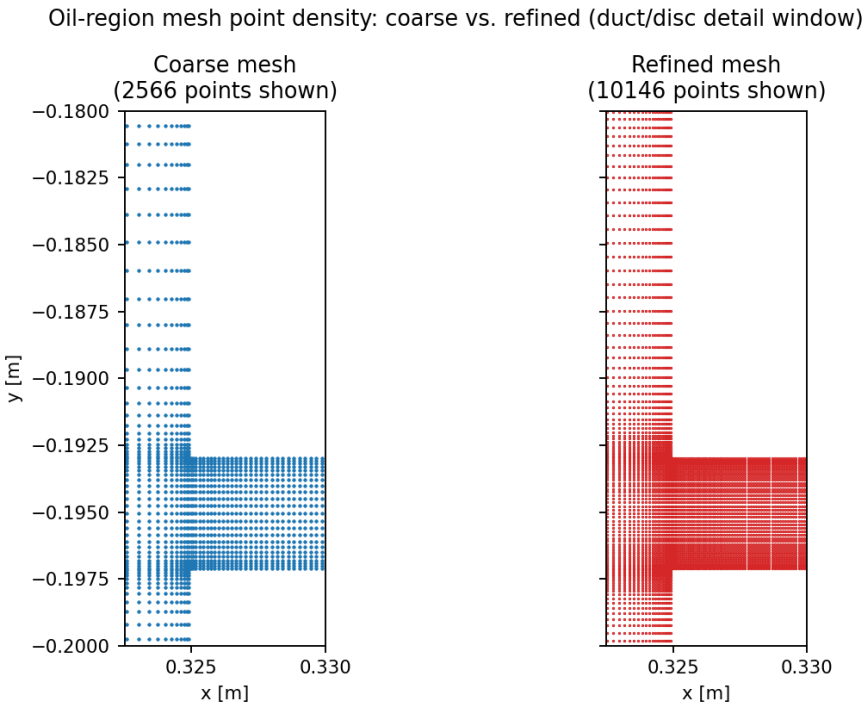


Figure 4.10: *Oil-region mesh point density in a shared duct/disc detail window, coarse mesh (left) versus refined mesh (right): the refined mesh shows the same duct-wall and axial-duct point distribution pattern at approximately 4x the local point density, confirming a uniform, not merely global, refinement.*

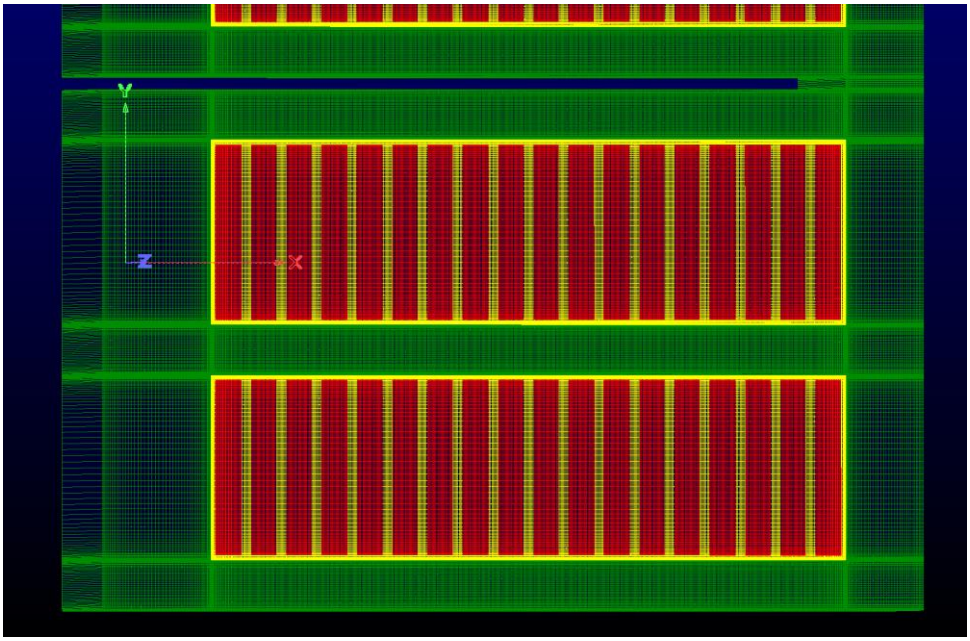


Figure 4.11: *Detail of the refined structured block topology around several adjacent discs (Pointwise).*

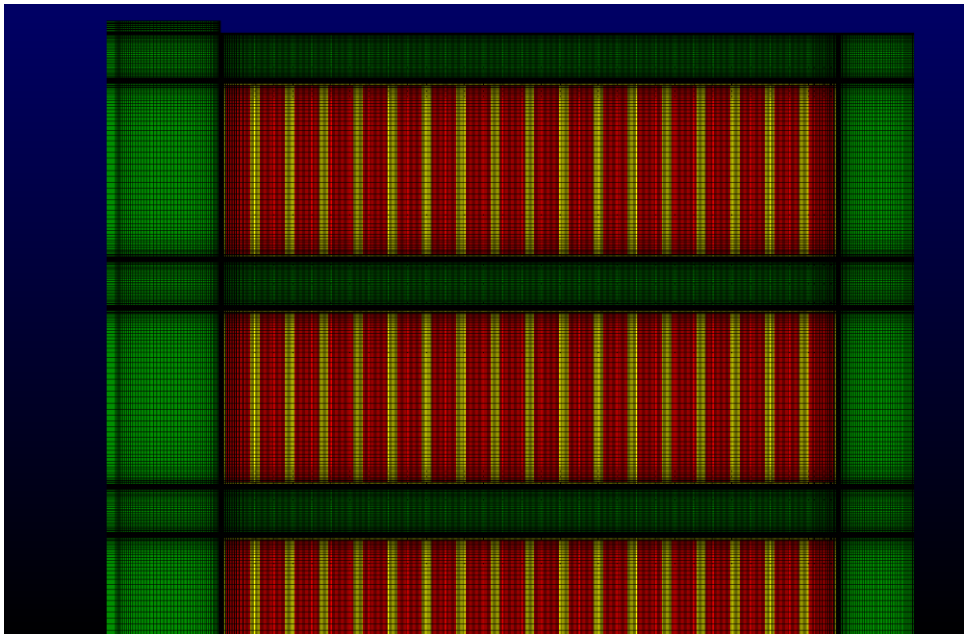


Figure 4.12: *Further detail of the refined mesh grading within a duct/disc region.*

4.6.1 Convergence history

The refined-mesh simulation was stopped before reaching a converged steady state. The available results were sufficient to verify the refined-mesh setup, including the region topology, boundary conditions, and mesh quality, but not to assess the final thermal behaviour.

The temperature field remained close to the initial and inlet condition, indicating that the solid regions had only begun to transfer heat to the bulk oil. Therefore, the refined-mesh case is presented as an early-stage result rather than a converged solution.

4.7 Discussion

Taken together, the coarse- and refined-mesh results support the conclusion that the porting of the single-pass model from foam-extend to OpenFOAM was successful in reproducing the underlying physics of the problem, and that the two computational meshes are constructed consistently with one another. On the coarse mesh, the production run to t = 947 067 produced strong agreement with the foam-extend reference: the fluid-region mean deviations settled at 0.25–1.08 K and the solid-region mean deviations at 4.28 K (copper) and 7.64 K (paper). Both the cumulative continuity error and the oil temperature range tightened monotonically over the run with no sign of a plateau at a physically incorrect state (Section 4.2.1), and the residual solid-region gap is fully consistent with the difference in relative run time between the two solvers set against the solids' much longer thermal time constant, not with a modelling or porting error. The coarse-mesh comparison presented in Section 4.4 is therefore treated as the primary, converged validation result of this chapter.

The refined mesh, by contrast, was stopped earlier, sufficient to confirm that the refined mesh, region topology and boundary conditions are set up correctly and consistently with the coarse mesh (Section 4.6), and that the solution is evolving smoothly and without any sign of instability or divergence, but explicitly not sufficient to reach anything resembling the coarse mesh's degree of thermal equilibration. Running the refined-mesh case to a comparable degree of convergence as the coarse mesh, either by continuing the existing run or by resuming from its current state with a longer time budget, is identified as the most immediate piece of further work arising from this chapter, and is discussed as such in Chapter 6.

Chapter 5

Two-Pass Extension: Variable-Properties and Boussinesq Comparison (Task 2)

5.1 Objectives and physical models

The second task of this thesis extends the single-pass model validated in Chapter 4 to a two-pass winding geometry. The same disc, cooling-duct, and paper-wrap arrangement described in Chapter 2 is used for both passes. The two passes are connected by a radial gap through which the oil flows from the first pass to the second. The model is then used to compare a constant-property Boussinesq model with a variable-thermophysical-properties model. Two thermophysical models were implemented using the same two-pass mesh, boundary conditions, and heat source. The main difference between the models is how the oil properties and buoyancy are treated. In the variable-properties (VP) model, the oil density, dynamic viscosity, thermal conductivity, and specific heat vary with temperature according to the polynomial correlations reported by Torriano:

$$k = 0.1509 - 7.101 \times 10^{-5} T$$
$$\rho = 1098.72 - 0.712T$$
$$\mu = 0.08467 - 4.0 \times 10^{-4} T + 5.0 \times 10^{-7} T^2$$
$$C_p = 807.163 + 3.58T$$

These temperature-dependent properties are implemented using OpenFOAM's native icoPolynomial thermophysical model. The copper region uses $k = 401$W m^{-1} K^{-1}, $\rho = 8933$kg m^{-3}, and $C_p = 385$J kg^{-1} K^{-1}. The paper region uses $k = 0.19$W m^{-1} K^{-1}, $\rho = 930$kg m^{-3}, and $C_p = 1340$J kg^{-1} K^{-1}.

In the Boussinesq model, the fluid properties are kept constant, and the buoyancy force is added separately using the custom-compiled libBoussinesqForce.so library provided by the supervisor. The reference values are $T_{\mathrm{ref}} = 336.67$K, $\beta = 8.29 \times 10^{-4}$K^{-1}, $\rho = 858.97$kg m^{-3}, $C_p = 2012.4$J kg^{-1} K^{-1}, $\mu = 6.684 \times 10^{-3}$Pa s, and $Pr \approx 105.9$.

Both models also use the limitTemperature fvOptions setting to keep the temperature within the range of 200–800 K during the simulation. This is included only as a safety measure. No cells reached either limit in the converged simulations, so the limiter did not affect the final results.

5.2 Two-pass mesh development

Two mesh-generation approaches were investigated. The first used OpenFOAM to trim and merge separate sub-meshes, with mapped-type boundaries connecting them at the internal junction. Although the mesh passed the standard geometric checks, long simulations showed a steadily increasing continuity error and eventually diverged. The problem was traced to mass conservation at the internal junction, so this approach was not used further. The final approach followed the same method validated in Task 1. A flat, two-dimensional mesh was first exported from Pointwise, and the wedge geometry was then added in OpenFOAM. The procedure was as follows:

1. A flat two-dimensional mesh was exported from Pointwise instead of exporting the angled wedge directly.
2. The wedge geometry was added using extrudeMesh with extrudeModel wedge, one cell layer, and an angle of 1°, giving 0.5°on each side.
3. The resulting mesh was checked using checkMesh -allTopology -allGeometry. A standard checkMesh without these options was not considered sufficient for the validation.
4. The mesh was divided into the oil, copper, and paper regions using splitMeshRegions -cellZonesOnly.
5. The mesh dimensions were converted from millimetres to metres using transformPoints -scale "(0.001 0.001 0.001)" for each region.
6. Each region was renumbered using renumberMesh -overwrite.
7. A final checkMesh -allTopology -allGeometry check was performed on each region.

The final mesh is a single continuous conformal mesh without an internal coupling junction. The coarse two-pass mesh contains 186,000 copper cells and 159,840 paper cells. These values are the same as those obtained from the earlier junction-based mesh for the same geometry, providing an internal check that the geometry and cell distribution were preserved.

5.3 Numerical setup and convergence criteria

Following a review of the preliminary results, the convergence criteria and linear-solver tolerances were tightened for all two-pass simulations. The residualControl limits for U, h, and p_{rgh}were set to 1×10^{-6}. The linear-solver tolerances for p_{rgh}, U, and $h$were also reduced to 1×10^{-12}, with relTol = 0.01. The relaxation factors were kept different for the two models. The VP case used $p_{rgh} = 0.2$, $U = 0.3$, and $h = 0.3$, while the more sensitive Boussinesq case used $p_{rgh} = 0.1$, $U = 0.15$, and $h = 0.2$. The outlet p_{rgh}boundary condition was also changed from a relative gauge value of zero to an ambient pressure of 1×10^5Pa, and the initial internal pressure field was set consistently with this value. For the incompressible formulation used here, this change does not affect the velocity or temperature solution because the pressure gradient is what influences the flow. It does, however, provide a clear and consistent pressure reference for the simulation.

5.3.1 Variable-properties (VP) model

The VP case uses OpenFOAM's icoPolynomial thermophysical model with the Torriano correlations for oil density, viscosity, thermal conductivity and specific heat as functions of temperature:

$\rho(T) = 1098.72 - 0.712 \cdot T$ [kg/m³]

$\mu(T) = 0.08467 - 4.0\times10^{-4} \cdot T + 5.0\times10^{-7} \cdot T^2$ [Pa·s]

$k(T) = 0.1509 - 7.101\times10^{-5} \cdot T$ [W/m·K]

$cp(T) = 807.163 + 3.58 \cdot T$ [J/kg·K]

Copper and paper properties are held constant (copper: ρ=8933, cp=385, k=401; paper: ρ=930, cp=1340, k=0.19), consistent with Chapter 4.

5.3.2 Boussinesq model

The Boussinesq model uses a constant-density rhoConst equation of state, while the buoyancy force is added separately through a compiled BoussinesqForce fvOptions library. A thermal expansion coefficient of $\beta = 8.29 \times 10^{-4}\ \mathrm{K}^{-1}$and a reference temperature of $T_0 = 336.67\mathrm{K}$ are used. The reference density is $\rho_0 = 858.97\ \mathrm{kg\ m}^{-3}$, the specific heat is $c_p = 2012.4\ \mathrm{J\ kg}^{-1}\mathrm{K}^{-1}$, and the dynamic viscosity is $\mu = 6.684 \times 10^{-3}$ Pa s, giving a Prandtl number of approximately 105.9. These values were compared with those reported by Salerno et al. for the same oil and geometry. The VP and Boussinesq models use the same mesh, boundary conditions, discretisation schemes, and solver relaxation settings. This keeps the numerical setup the same for both cases and allows the differences in their results to be examined mainly in terms of the two modelling approaches.

5.4 Heat-source correction

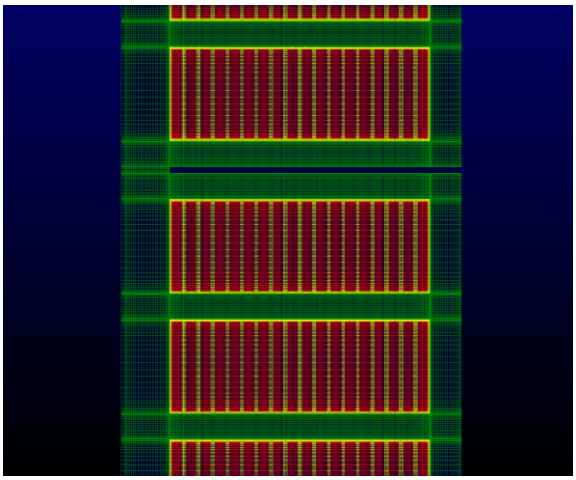
The original two-pass simulations used the same total heat source as the single-pass case, 157.943 W. This was not appropriate for the two-pass geometry, which contains more discs and therefore more copper. Although the simulations reached numerical convergence, they produced unrealistic temperature distributions, with the hotspot appearing near the middle of the winding instead of closer to the outlet. The corrected heat source was calculated from the heat generated per disc in the single-pass case. The total single-pass heat source of 157.943 W was distributed over 21 discs, giving approximately 7.521 W per disc. The two-pass geometry contains 40 discs in total: 21 in the first pass, including the two entry-region discs, and 19 in the second pass. The total heat source was therefore set to

$$7.521 \times 40 = 300.844\ \mathrm{W}.$$

The value was also checked using the copper cell counts. The ratio between the two-pass and single-pass copper cell counts is $186{,}000/97{,}650 \approx 1.9$, which is consistent with the increase in the number of discs and supports the corrected total heat source.

5.5 Mesh

The coarse two-pass mesh contains 354,906 cells in the fluid region, 186,000 cells in the copper region, and 159,840 cells in the paper region. The copper and paper cell counts are consistent with the single-pass coarse mesh when scaled by the ratio of discs, $40/21 \approx 1.905$, showing that the two-pass mesh keeps the same basic mesh structure for each disc. The computational domain extends from $x = 0.4162$to $0.4837\mathrm{m}$ in the radial direction and from $y = -0.0041$to $0.7792\mathrm{m}$ in the axial direction, covering the complete two-pass stack.



Detail of the structured block topology around adjacent discs: copper conductors (red), paper wrap (yellow) and oil ducts (green)

5.6 Convergence Behaviour

Both simulations were run using a copper heat source of 300.844 W and a p_{rgh}outlet boundary condition of 1×10^5Pa. The VP case reached a simulated time of $t = 756{,}800$, while the Boussinesq case reached $t = 727{,}000$. During the simulations, the fluid temperature in both cases remained within a stable and physically realistic range. The VP case reached temperatures from 319.85 K to 368.98 K, while the Boussinesq case ranged from 319.85 K to 373.41 K. These temperature ranges are consistent with the heat generated in the winding being removed by natural convection. The stable and bounded temperature fields indicate that both simulations reached a physically consistent thermal state.

5.7 Task 2a: VP vs. Boussinesq Comparison

Quantitative comparison between the VP and Boussinesq solutions was carried out using the same three sampling lines as the spatial field comparison. These were a vertical line through the inner channel at $x = 0.4172$m, a vertical line through the outer channel at $x = 0.4827$m, and a horizontal line at $y = 0.39$m passing through the copper, paper, and adjacent oil regions of a disc. The compared fields were temperature T, velocity magnitude $|\ U\ |$, density ρ, and pressure.

5.7.1 Quantitative agreement

Line	mean |ΔT| [K]	max |ΔT| [K]	mean |ΔU| [m/s]	max |ΔU| [m/s]	mean |Δρ| [kg/m³]	max |Δρ| [kg/m³]
Inner channel	0.01	0.03	2.8×10^{-4}	7.8×10^{-4}	10.5	12.0
Outer channel	0.13	0.72	4.9×10^{-4}	3.6×10^{-3}	7.0	12.0
Horizontal (disc)	0.25	3.18	8.1×10^{-4}	3.1×10^{-3}	9.1	12.0

Table 5.1: *Point-by-point VP-vs-Boussinesq agreement along the three sampling lines (coarse mesh, converged/near-converged states).*

Temperature and velocity show very close agreement between the two models along all three sampling lines. The mean temperature difference is only 0.01–0.25 K, compared with a total oil temperature rise of about 49 K. The differences in velocity are also very small, being roughly two orders of magnitude lower than the characteristic flow velocity.

The density values are different because the two models treat density differently. The Boussinesq model uses a constant density of 858.97 kg/m³, while the VP model calculates density according to the local temperature. As a result, the mean absolute density difference is about 7–11 kg/m³, with a maximum difference of approximately 12 kg/m³ along the three sampling lines.

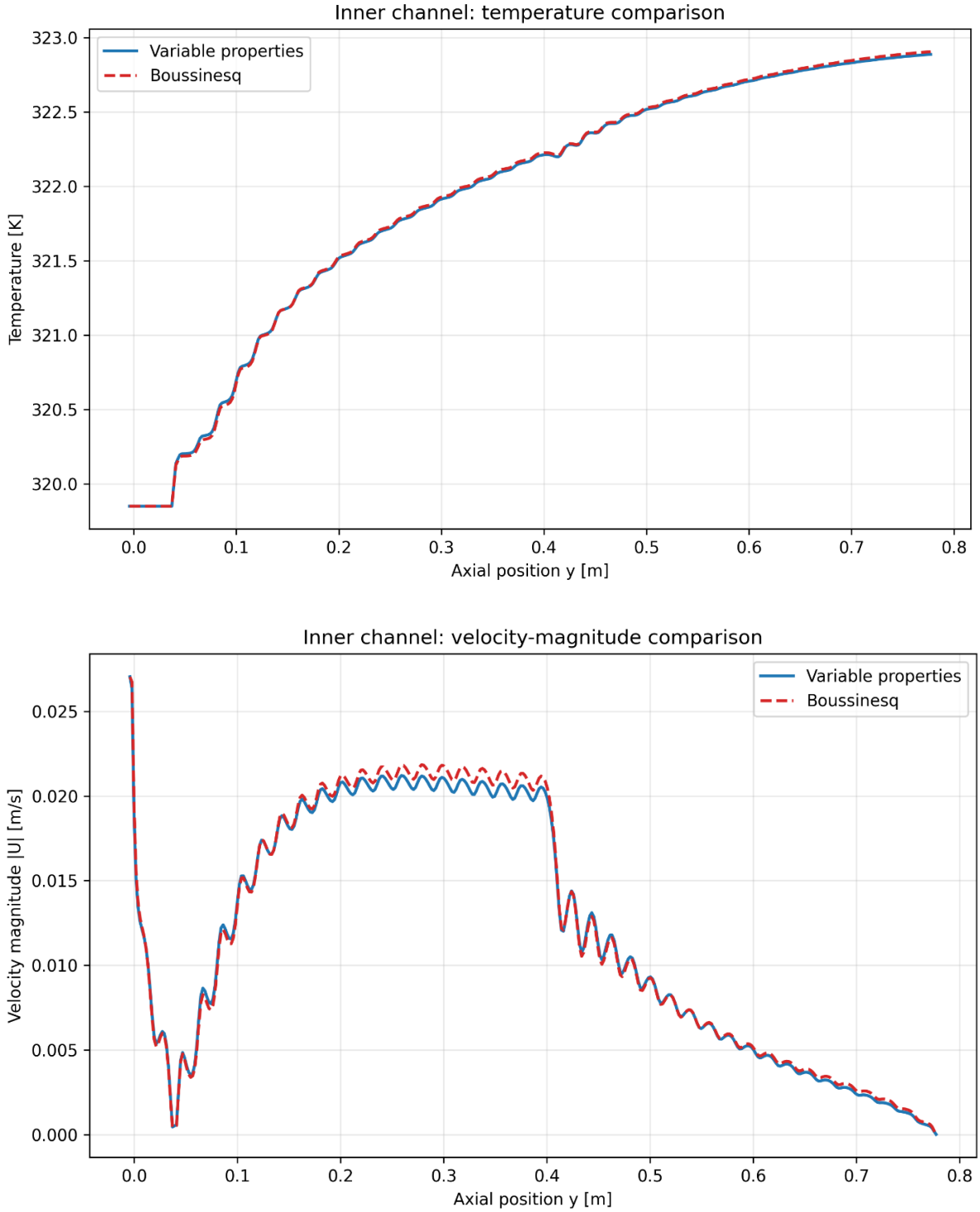


Figure 5.1: *VP (solid) vs. Boussinesq (dashed) comparison along the inner-channel line: temperature, velocity magnitude*

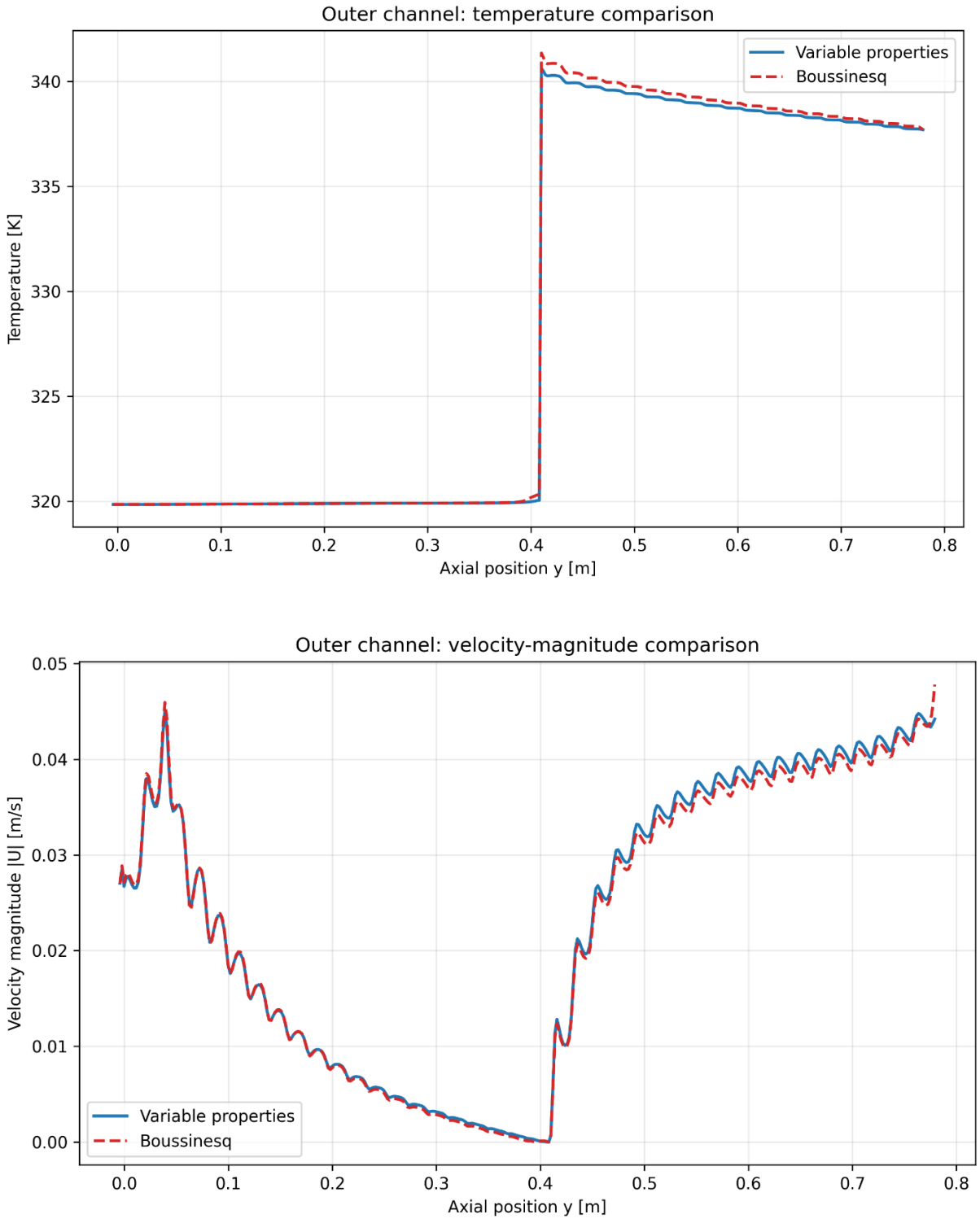


Figure 5.2: *VP vs. Boussinesq comparison along the outer-channel line.*

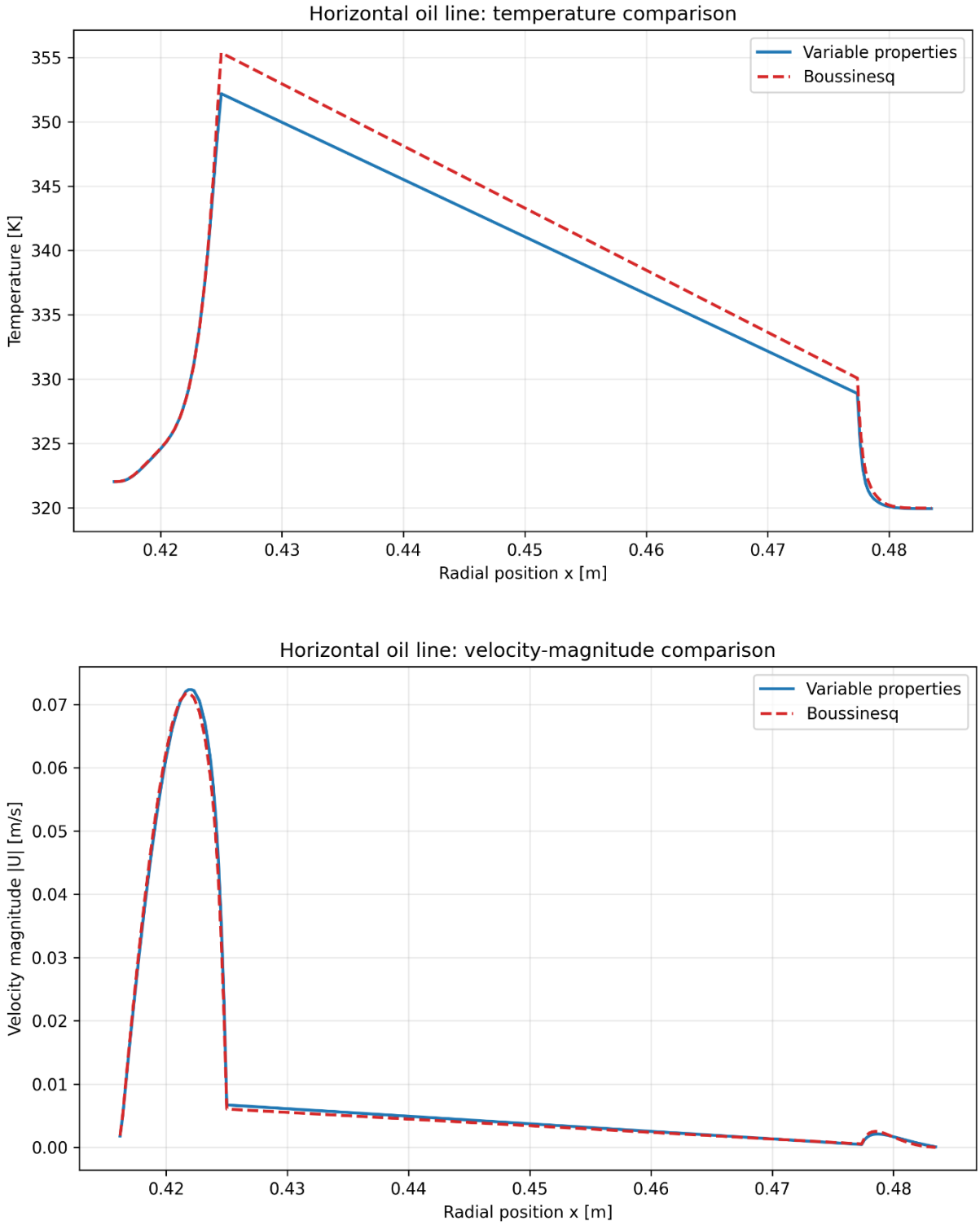


Figure 5.3: *VP vs. Boussinesq comparison along the horizontal line, oil sub-domains only.*

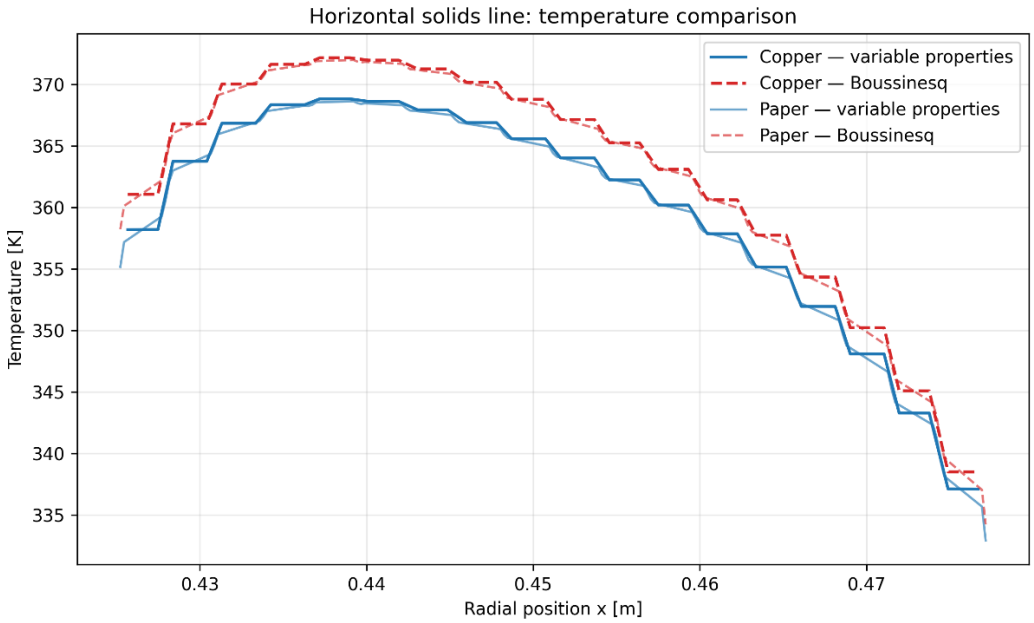


Figure 5.4: *Copper and paper temperature along the same horizontal line, VP vs. Boussinesq.*

5.7.2 Field contours

Figures 5.5–5.12 show full-domain field contours for both cases, rendered directly from the exported VTK data.

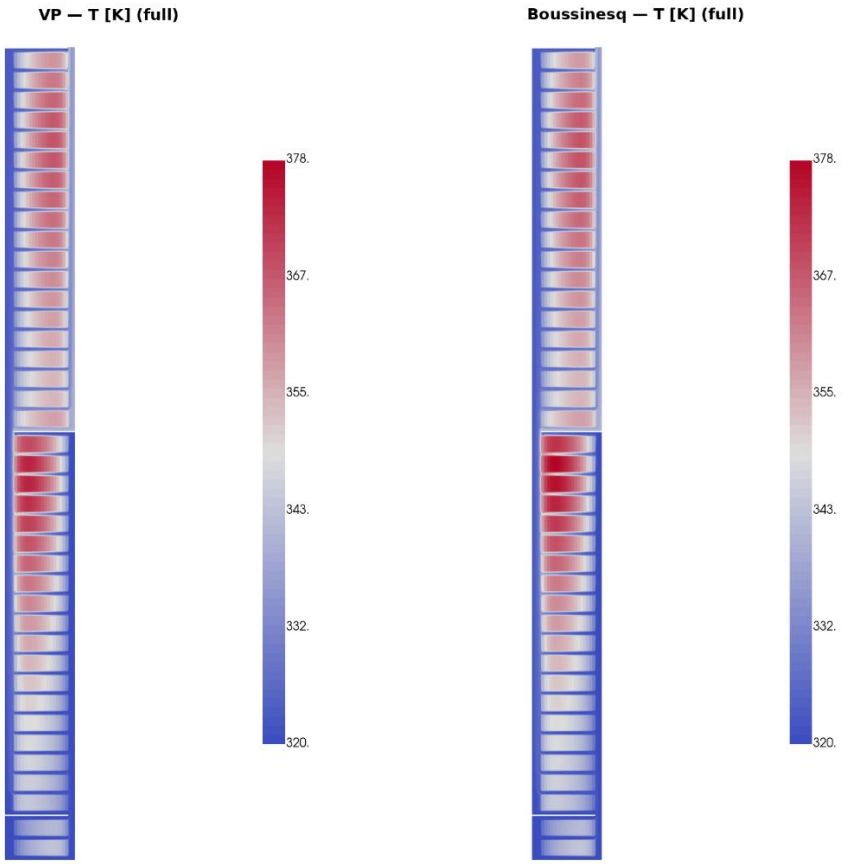


Figure 5.5 / 5.6: *Full-domain temperature contour: VP and Boussinesq.*

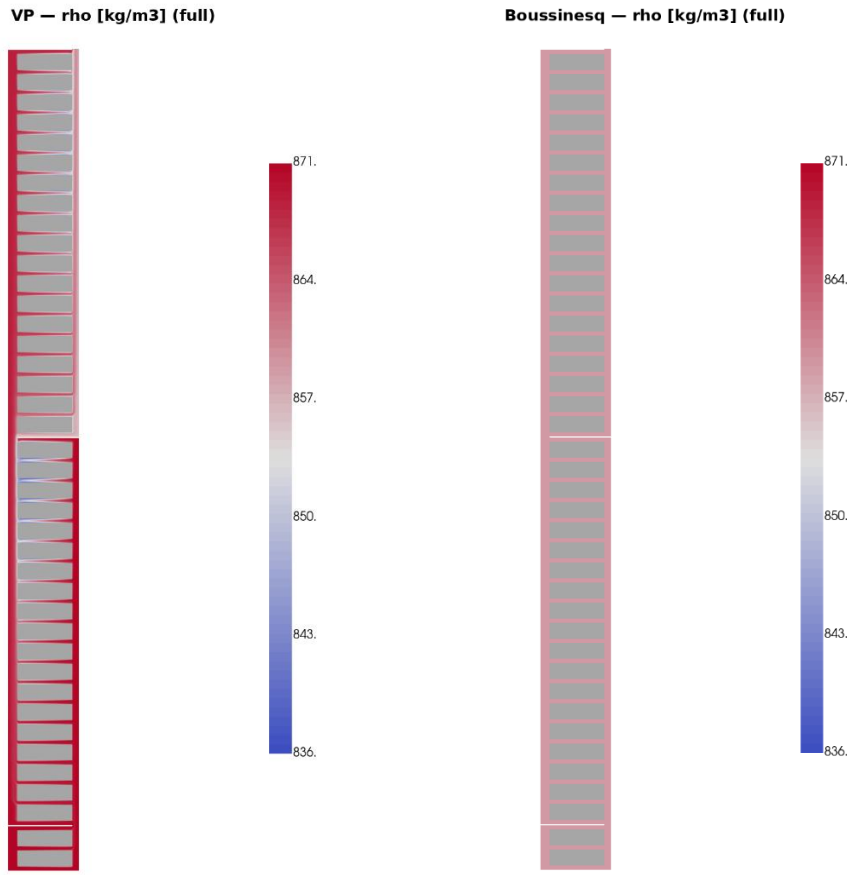


Figure 5.7 / 5.8: *Full-domain density contour: VP and Boussinesq.*

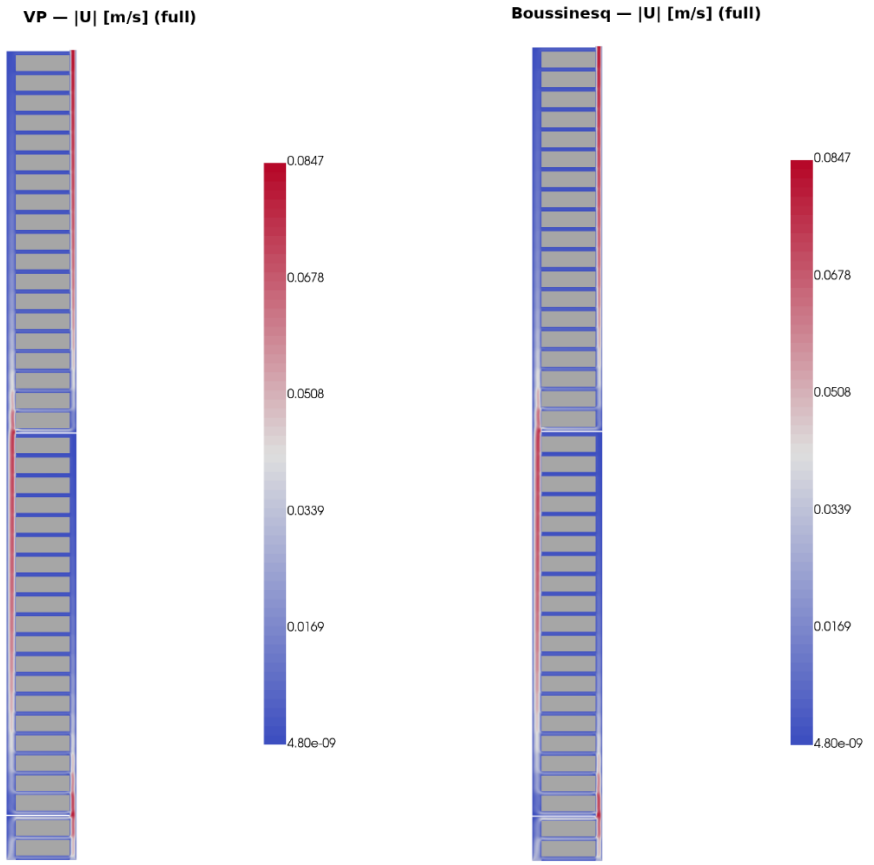


Figure 5.9 / 5.10: *velocity-magnitude contour: VP and Boussinesq.*

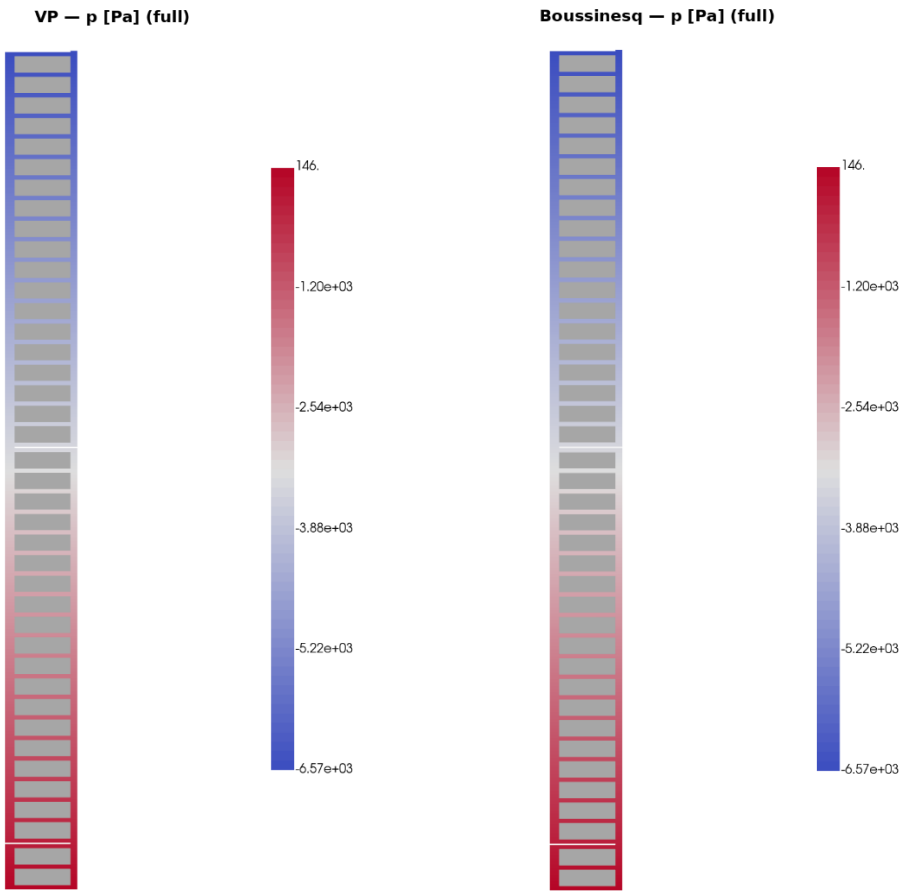


Figure 5.11 / 5.12: *pressure contour: VP and Boussinesq*

The temperature contours show a smooth increase in temperature along both passes. This is consistent with the oil gaining heat as it moves upward through the duct stack. The highest disc temperatures are approximately 374 K for the VP model and 378 K for the Boussinesq model, occurring near the end of each pass, just before the oil enters the return duct. No unusually hot individual disc is observed, and the overall temperature distribution is similar in both simulations.

5.8 Task 2b: Analytical Boussinesq Validity Assessment

Task 2a's comparison shows the two models agree closely in the flow field they predict, but agreement in the numerical output is not, by itself, a formal validity check. Task 2b addresses this by comparing the simulation results against the analytical validity criterion of Gray and Giorgini (1976), the standard reference for this assessment, and the one already cited in the Salerno et al. papers that this thesis's case study is drawn from.

5.8.1 Criterion

Gray and Giorgini describe each fluid property ϕ, including density ρ, viscosity μ, specific heat c_p, and thermal conductivity k, as a linear variation around a reference state:

$$\frac{\phi}{\phi_0} = 1 + \varepsilon_{\phi,T}\frac{T - T_0}{\Delta T} + \varepsilon_{\phi,P}\frac{P - P_0}{\rho_0 g L}$$

The Boussinesq approximation is considered valid within an accuracy $\hat{\sigma}$when $\varepsilon_{\phi,T} < \hat{\sigma}$for every fluid property ϕ. Two additional energetic terms must also remain below the same limit: the pressure-work term, proportional to $\beta g L T_0/c_p$, and the viscous-dissipation term, proportional to $\beta g L\, Pr/c_p$. Following Gray and Giorgini, three tolerance levels are considered in this study: 5%, 10%, and 20%. The property variations were calculated from the Torriano correlations using two temperature ranges obtained from the VP simulation. The first is the **bulk range**, approximately 320–355 K, which represents the fluid in the main flow region along the three comparison lines. The second is the **global range**, approximately 320–369 K, which represents the full fluid domain, including the thin thermal boundary layer near the hottest disc surfaces.

Property	εφ,T (bulk)	εφ,T (global)	5% (bulk / global)	10% (bulk / global)	20% (bulk / global)
ρ (density)	2.9%	4.1%	valid / valid	valid / valid	valid / valid
μ (viscosity)	33.1%	40.9%	violated / violated	violated / violated	violated / violated
k (conductivity)	2.0%	2.8%	valid / valid	valid / valid	valid / valid
cp (specific heat)	6.3%	8.7%	violated / violated	valid / valid	valid / valid
Pressure-work term	<0.01%	<0.01%	valid / valid	valid / valid	valid / valid
Viscous-dissipation term	0.03%	0.03%	valid / valid	valid / valid	valid / valid

Table 5.2: *Gray & Giorgini (1976) property-variation and energetic criteria, evaluated for the two-pass coarse-mesh case.*

5.8.2 Interpretation

The formal criterion is satisfied for density and thermal conductivity at all three thresholds, both in the bulk flow and in the near-wall region close to the hottest discs. The peak fluid temperature is approximately 369 K, which gives realistic property variations over the operating range.

Viscosity shows a different behaviour. It exceeds the allowed variation at all three thresholds, both in the bulk and near the wall. This is mainly because the viscosity of mineral transformer oil is much more sensitive to temperature than its density or thermal conductivity over this temperature range. Therefore, viscosity is the main property that causes the overall criterion to be violated when all four properties are considered together, as required by the Gray and Giorgini criterion. Specific heat exceeds the limit only at the 5% threshold, while it remains within the limit at the 10% and 20% thresholds. The two energetic terms show only very small variations and do not affect the overall assessment.

The results also show that the VP and Boussinesq models produce very similar temperature and velocity fields, even though the formal validity criterion is not satisfied. This can be explained by the role of viscosity in the governing equations. Viscosity affects the flow through diffusion and Reynolds-number scaling, whereas the Boussinesq approximation mainly modifies the buoyancy term. Therefore, a relatively large variation in viscosity does not necessarily lead to a large difference between the predicted temperature

and velocity fields, even though it is sufficient to make the approximation formally invalid according to the Gray and Giorgini criterion. This behaviour is also consistent with the results reported by Salerno et al. for the same case study and transformer oil.

5.9 Discussion

Taken together, Sections 5.7 and 5.8 show two aspects of the Boussinesq approximation. In terms of the calculated flow field, the Boussinesq model gives temperature and velocity results that are very close to the variable-properties model across the two-pass domain, including near the hottest discs. However, when the formal Gray and Giorgini criterion is applied to all four thermophysical properties, the approximation is not fully valid.

Density and thermal conductivity remain within the required limits at all three thresholds across the domain, including the near-wall region. Specific heat is within the limit at the 10% and 20% thresholds, but not at 5%. Viscosity is the only property that exceeds the limit at all three thresholds, both in the bulk flow and near the wall, because its variation with temperature is relatively large.

Therefore, for this two-pass case, the Boussinesq approximation provides very similar bulk temperature and flow predictions to the variable-properties model. However, according to the formal criterion, its validity is limited by the temperature dependence of oil viscosity. This distinction should be kept clear when interpreting the results of the two-pass study.

5.10 Refined Mesh:

A refined two-pass mesh was built using the same extrudeMesh-based procedure. The heat source was set to 300.844 W, and the p_{rgh}outlet boundary condition was set to 1×10^5Pa. The refined mesh contains 1,450,034 cells in the fluid region, 776,000 in the copper region, and 649,600 in the paper region. This corresponds to approximately 4.1 times the number of cells in each region compared with the coarse mesh, while keeping the same geometry.Due to the limited time available before submission, the refined-mesh VP and Boussinesq simulations could not be run until convergence. so the results presented here are early-transient snapshots: the VP case at $t = 3{,}900$and the Boussinesq case at $t = 2{,}540$. These times are much shorter than the simulation ranges required for the coarse-mesh cases to reach convergence, as discussed in Section 5.6. The same approach was used for the refined mesh in Task 1, where the results were also presented as an early transient rather than as a converged solution.The purpose of these results is to confirm that the refined mesh and numerical setup are working correctly and that the simulations produce physically reasonable early-transient behaviour. They are not used to draw conclusions about the validity of the Boussinesq approximation, since such conclusions require fully converged results.At this stage, both simulations remain close to the inlet and initial temperature of 319.85 K, and only limited heating has occurred in the oil and solid regions. The Boussinesq case reaches a minimum fluid temperature of 316.23 K, which is slightly below the inlet value and is consistent with the early stage of the simulation. The available results are therefore not sufficient for a meaningful comparison between the VP and Boussinesq models, detailed spatial analysis, or a Gray and Giorgini validity assessment.

5.10.1 Field contours

Figures 5.13–5.18 show the same full-domain fields presented in Section 5.7.2, but for the refined mesh. The nearly uniform colour across most of the fields is expected because these results are from an early stage of the simulation. The temperature and flow fields have not yet developed the spatial variations observed in the converged coarse mesh results.

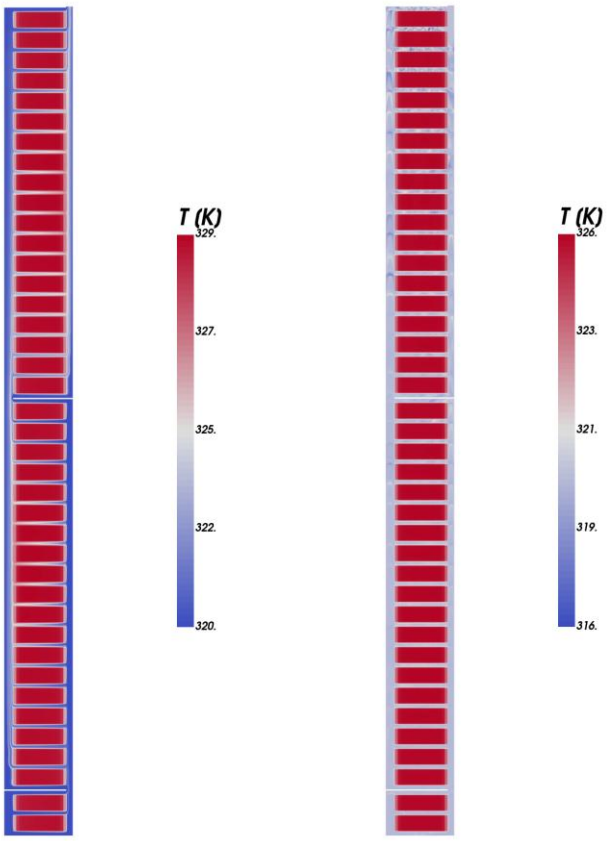


Figure 5.13 / 5.14: *Full-domain temperature contour, refined mesh: VP and Boussinesq. Near-uniform colouring reflects the early-transient state.*

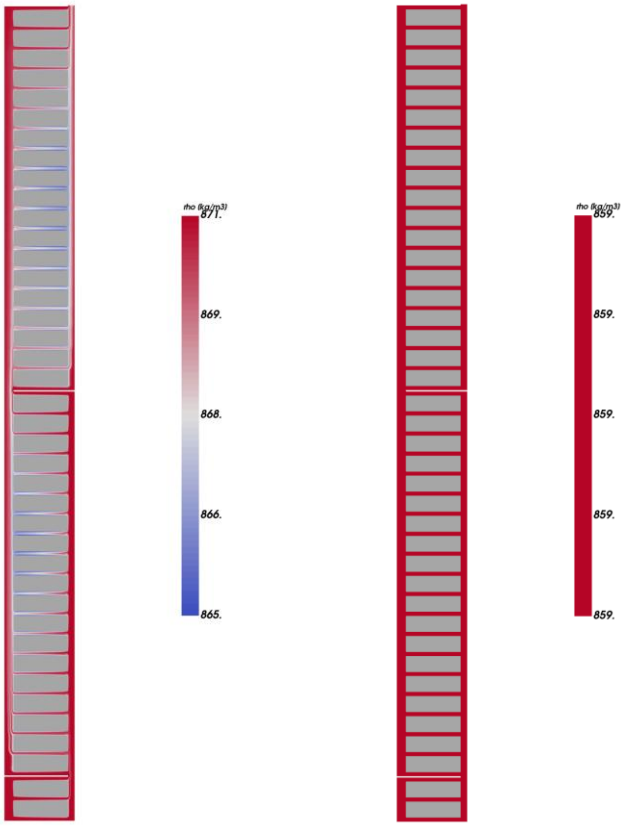


Figure 5.15 / 5.16: *Full-domain density contour, refined mesh: VP (minimal variation so far) and Boussinesq (constant).*

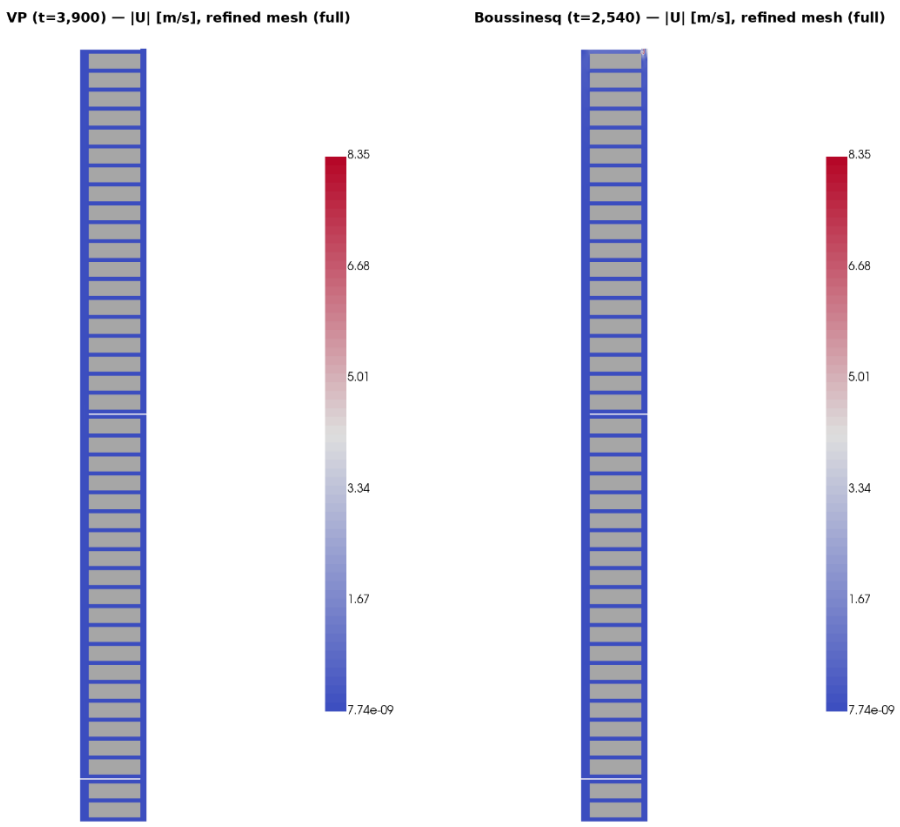


Figure 5.17 / 5.18: *Full-domain velocity contour, refined mesh: VP and Boussinesq.*

5.10.2 Why no Task 2b assessment yet

A Gray and Giorgini validity table, as used in Section 5.8, is not included for the refined mesh. The criterion is intended to be evaluated over the temperature range reached by the simulation. At this stage, the fluid temperature ranges from 319.77–328.52 K for the VP case and 316.23–323.71 K for the Boussinesq case. These ranges represent only an early stage of the simulation and are not yet representative of the final operating condition.

For this reason, calculating the property-variation values from the current temperature range would not provide a meaningful assessment of the Boussinesq approximation. The refined-mesh validity analysis is therefore left for a later stage, once the simulations have progressed far enough to reach a representative thermal state.

The refined-mesh results are consequently presented as a verified but not-yet-converged extension of the coarse-mesh study. The mesh, simulation setup, and post-processing procedure have been successfully established, while the current field results are reported as early-transient data.

5.11 Summary

Both required Task 2a simulations, using variable thermophysical properties and the Boussinesq approximation, were completed on the corrected coarse two-pass mesh and compared directly. The Boussinesq case reached a well-converged state, while the VP case was close to a stable final state but had not completely plateaued at the last available result.

The two models produced very similar temperature and velocity fields, with mean temperature differences of only 0.01–0.25 K. Density shows a systematic difference between the two models, as expected from the different treatment of thermophysical properties, but it remains within the Gray and Giorgini criterion throughout the domain, including near the hottest disc surfaces.

The Gray and Giorgini assessment in Task 2b shows that the Boussinesq approximation is not formally valid when all thermophysical properties are considered together. However, density and thermal conductivity satisfy the criterion at all thresholds, while the temperature dependence of oil viscosity is the main factor responsible for the formal violation. This shows why checking density alone is not sufficient when assessing the approximation.

The coarse-mesh study is therefore complete. A refined two-pass mesh, containing approximately 4.1 times the number of cells of the coarse mesh, was also constructed and verified using the same setup. The refined simulations were not run to convergence before submission, so their early-transient results are presented separately in Section 5.10 as preliminary results. A fully converged refined-mesh comparison and the corresponding Gray and Giorgini assessment remain as the next stage of the study.

Chapter 6

Conclusions

6.1 Summary of findings

This thesis presents the porting of a conjugate heat transfer model of an oil-immersed transformer low-voltage disc winding from foam-extend 4.0 to OpenFOAM v2306. The model was first studied for a single-pass geometry and then extended to a two-pass geometry to compare a constant-property Boussinesq model with a variable-thermophysical-properties model and to assess the validity of the Boussinesq approximation.

The single-pass study, presented in Chapter 4, was validated on the coarse mesh. The mean temperature difference in the fluid region was 0.25–1.08 K, while the mean differences in the copper and paper regions were 4.28 K and 7.64 K, respectively, compared with the fully converged foam-extend reference. The remaining difference in the solid regions is explained by the different simulation times and the much longer thermal response of the solid regions, rather than by an error in the model or its implementation. The refined single-pass mesh was only run to an early transient state at $t = 4646$s. It confirmed that the mesh, region topology and boundary conditions were set up correctly and consistently with the coarse mesh. The larger solid-region differences of 32.96–33.40 K on average, with a maximum of 37.05 K, are therefore associated with the simulation state and elapsed run time rather than with a mesh-sensitivity problem. A direct mesh-independence comparison cannot yet be made from these results.

A specific meshing procedure was also developed for creating OpenFOAM-compatible axisymmetric wedge meshes from Pointwise exports. The procedure uses a flat mesh exported from Pointwise and adds the wedge angle afterwards using OpenFOAM's extrudeMesh utility, instead of exporting the angled wedge directly from Pointwise. This approach, together with the other practical OpenFOAM lessons described in Chapter 3, can be reused in future work and was also used for the two-pass mesh in Chapter 5.

The two-pass extension, presented in Chapter 5, required a total heat source of 300.844 W, corresponding to 7.521 W per disc for 40 discs. On the coarse mesh, the Boussinesq simulation reached a well-converged state, while the variable-properties simulation was close to a stable final state but had not completely plateaued. The two models produced very similar temperature and velocity fields along all three sampling lines, with mean temperature differences of 0.01–0.25 K over a total oil temperature rise of about 49 K. The density values differ systematically because the two models treat density differently. The Boussinesq model uses a constant density of 858.97 kg/m³, while the variable-properties model calculates density from the local temperature. The resulting mean absolute density difference is about 7–11 kg/m³, with a maximum of approximately 12 kg/m³ along the three sampling lines.

The Task 2b assessment used the Gray and Giorgini (1976) criterion and considered all four thermophysical properties rather than density alone. The results show that the Boussinesq approximation is not formally valid over the two-pass domain because of the strong temperature dependence of mineral-oil viscosity. Viscosity varies by approximately 33–41%, exceeding all of the benchmark tolerances. Density and thermal conductivity remain within the required limits at all thresholds, including near the hottest disc surfaces, while the two energetic terms show negligible variation. Despite this formal limitation, the Boussinesq and variable-properties models produce very similar temperature and velocity fields. This is because viscosity affects the governing equations through diffusion and Reynolds-number scaling, while the Boussinesq approximation mainly modifies the buoyancy term. Therefore, the formal criterion and the numerical comparison provide different types of information. This behaviour is also consistent with the results reported by Salerno et al. for the same case study and oil.

Finally, a refined two-pass mesh containing approximately 4.1 times the coarse-mesh cell count was built using the same modelling approach. The corrected heat source and pressure boundary condition were included from the beginning, and the complete comparison procedure, including spatial sampling, comparison plots and field contours, was successfully applied to the refined mesh. However, the refined simulations remained at an early transient stage because cluster access was not available before the submission deadline. The results presented in Section 5.10 are therefore preliminary and are not sufficient to draw conclusions about the refined-mesh Task 2a comparison or the Gray and Giorgini validity assessment.

6.2 Future work

Continue the Task 1 refined-mesh simulation until it reaches a level of convergence comparable to the coarse-mesh case. This will provide a proper assessment of mesh sensitivity in addition to the coarse-mesh validation presented in Chapter 4.

Allow the Task 2a coarse-mesh variable-properties simulation in Section 5.6 to continue until the cumulative continuity error and \(p_{rgh}\) residual reach a stable plateau comparable to that obtained for the Boussinesq case.

Complete the Task 2 refined-mesh simulations for both the variable-properties and Boussinesq models. The simulations should be run to a level of convergence comparable to the coarse-mesh cases, preferably using a computing cluster. The early-transient results currently presented in Section 5.10 can then be replaced with converged comparison graphs, field contours and tables.

Once the refined Task 2 simulations have converged, repeat the Task 2a quantitative comparison, including average disc temperature for each pass, mass-flow-rate distribution among the cooling ducts, and hot-spot location and magnitude, following the methodology of Salerno et al. The Gray and Giorgini validity assessment from Task 2b should also be repeated using the refined-mesh results..

Bibliography

[1] F. Torriano, M. Chaaban, P. Picher, “Numerical study of parameters affecting the temperature distribution in a disc-type transformer winding,” Applied Thermal Engineering, vol. 30, no. 14–15, 2010.

[2] A. Salerno, A. Leonforte, D. Angeli, M. A. Corticelli, et al., “CFD analysis of natural convection oil flow in a transformer winding,” Journal of Physics: Conference Series, vol. 1868, 012031, 2021.

[3] A. Salerno, A. Leonforte, D. Angeli, M. A. Corticelli, et al., “Assessment of the Boussinesq approximation for the CFD simulation of natural convection cooling in transformer windings,” Applied Sciences, vol. 14, no. 21, 9736, 2024.

[4] D. D. Gray, A. Giorgini, “The validity of the Boussinesq approximation for liquids and gases,” International Journal of Heat and Mass Transfer, vol. 19, no. 5, 1976.

[5] IEC 60076-7, “Power transformers, Part 7: Loading guide for mineral-oil-immersed power transformers,” International Electrotechnical Commission.

[6] IEEE C57.91, “IEEE Guide for Loading Mineral-Oil-Immersed Transformers and Step-Voltage Regulators,” Institute of Electrical and Electronics Engineers.

[7] A. Vezzani, “Analisi CFD dell’avvolgimento di bassa tensione di un trasformatore di potenza immerso in olio,” M.Sc. thesis, Università degli Studi di Modena e Reggio Emilia, 2021, used as a structural reference for the present thesis, prepared within the same research group.

[8] OpenFOAM Foundation, OpenFOAM v2306 User Guide, 2023.

[9] Pointwise Inc., Pointwise Reference Manual.

[10] S. V. Kulkarni, S. A. Khaparde, “Transformer Engineering: Design, Technology, and Diagnostics,” 2nd ed., CRC Press, 2013. Source for the core-loss relations and typical operating flux-density and lamination figures cited in Section 1.1.2.